TRABAJO FIN DE MÁSTER

IMPROVING INSTRUMENTAL POLARIZATION DETERMINATION IN SENSITIVE RADIO INTERFEROMETERS: THE CASE OF B1933+6648

María Arias de Saavedra Benítez

Supervisado por
Antxon Alberdi Odriozola (IAA-CSIC)

Septiembre de 2015

Contents

Introduction

The polarization of radiation from an astronomical source is a key observable to probe physical processes occurring in the emitting regions, and provides information that is not obtainable from total intensity observations. For instance, linear polarization observations of a synchrotron source, such as a relativistic jet, measure the degree of order in a magnetic field and its orientation, contributing to the understanding of jet formation, collimation, and acceleration. Multiwavelength observations add information about the opacity and Faraday depth of an emitting region, and can set limits on the low energy end of the electron energy spectrum. They can also play an important role in the discovery and analysis of gravitationally lensed sources [14].

Polarization sensitive interferometric observations at subarcsecond resolutions, therefore, can have profound implications for theories of compact radio sources. To achieve the resolutions required for the study of these objects, it is necessary to resort to interferometers with very long baselines.

The angular resolution of a single-dish radio telescope is $\sim \lambda/D$, where D is the diameter of the dish; for an interferometer, the angular resolution is $\sim \lambda/B$, where B is the longest baseline between the antennas. In addition to improving the resolution that an observer can achieve by several orders of magnitude, interferometers comprising $N \geq 2$ moderately small dishes have mitigated many practical problems associated with single dishes, such as tracking accuracy, limits on collecting area, vulnerability to fluctuations in atmospheric emission and receiver gain, radio-frequency interference, and pointing shifts caused by atmospheric refraction [1].

For continuum observations, the signal-to-noise ratio depends (among others) on the inverse of the square root of the bandwidth ($SNR \propto BW^{-1/2}$); larger bandwidths are preferred because they improve the sensitivity of the telescope. An important disadvantage in the use of interferometers has typically been that their total bandwidths and number of simultaneous frequency channels were lower than those of single dishes. However, recent advances in digital correlator electronics have largely overcome these practical limitations, so interferometers are playing an increasingly dominant role in observational radio astronomy [1].

Technological improvements are increasing the bandwidths at which interferometers can observe (and hence their sensitivity) yet often it is not clear what is the best approach for analyzing the data taken with these upgraded instruments.

Such is the case for polarization measurements. Their main difficulty is that frequently the source polarization is of the order of the intrinsic instrumental polarization due to imperfections of the feed. This works seeks to address the question of what is the best strategy to remove instrumental polarization for large bandwidth experiments. If instrumental polarization depends on frequency, the calibration of instrumental polarization cannot be done jointly for the entire

bandwidth, and needs a more careful treatment on small frequency segments.

In order to address this question, we use observations taken with the eMERLIN interferometer of the gravitationally lensed source B1938+6648. We calibrate the instrumental polarization according to two different methods: integrating the instrumental polarization values for each subband, and for each channel within a single subband. We conclude that the correction per channel produces polarization image with a lower noise than the image corrected per subband by a factor of four, and is thus the better choice. From the point of view of the astrophysical source of the lens B1938+6648, we present new epoch observations, with polarization percentage and angle values, and suggest that certain components are repeated images of a single, unlensed object. We also report that some variability has taken place on the source from the earlier epochs observations.

Chapter 1

Polarization in radio interferometry

The polarization properties of a radio source are a good signature of its emission mechanism. Polarization measurements at radio frequencies are relatively simple to make, and so polarization images are made routinely. However, there are several issues to take into account when it comes to the calibration of instrumental polarization.

In this section, I will discuss polarization in the context of radio astronomy, and how measurements are taken in radio interferometric arrays. I will also explain the calibration process, whereby the response of the instrument is derived from observations of sources with known flux, shape, and spectrum.

1.1 Radio Interferometry

In the case of single-dish radio astronomy, the collecting area of the dish dictates the faintness of objects it can reveal, and the resolving power (which is directly related to the dish diameter) determines to what detail they can be discerned. Radio telescopes work at the diffraction limit.

It can be useful to think of a telescope as a Fourier filter. Via the Fourier transform, the intensity distribution of a radio source can be represented as a spectrum of sinusoidal waves of differing frequencies, each frequency component having an amplitude and a phase. Scanning a dish antenna across a source has the effect of a low-pass filter applied to the transform, eliminating all Fourier components above a maximum that depends on the size of the dish. If the dish has W wavelengths (D/λ) across it, then only Fourier components below W cycles/radian are passed. A smaller source has a wider transform, so to see more detail we need a way to register the higher Fourier components in the transform [11].

A **radio interferometer** is a an array of radio telescopes that observe jointly. Aperture synthesis is used to make images with the resolution of a single dish that had the aperture of the longest interferometric baseline.

An interferometer is sensitive to a range of angular sizes ($\lambda/B_{max} \leq \theta \leq \lambda/B_{min}$, where B_{max} and B_{min} are the maximum and minimum separation between the apertures). The field of view (FoV) of an individual pointing is in fact the beam size of the antenna with the largest diameter $\theta_f \approx \theta_{bm} \approx \lambda/D_{max}$, and it depends inversely on integration time and bandwidth for the basic interferometric data (large integration times and bandwidths smear the FoV [1]). The interferometer

[1] This is managed with input `NCHAV` in `AIPS` task `IMAGR`.

acts as a band-pass filter of the Fourier components of the intensity distribution of the radio source. An interferometer does not have the collecting area of a single dish of equivalent size, and so it cannot recover the total flux of resolved sources, except if the source is compact (unresolved) at all angular scales.

Interferometry makes use of the interference pattern produced by two or more spaced receiving apertures pointed towards a source. By multiplying (correlating) the measured voltages generated at the telescope apertures, directly or with a given delay, we obtain the interferometric fringe amplitudes and phases. The fringe phase is related to the source's positional offset from a reference position. At the end of the observing session we have both an amplitude and a phase for each measured Fourier component of the brightness distribution. A single dish only records an amplitude, and so in order to make images it must point at different locations of the source, and each pointing is a data point. Measuring amplitudes *and* phases allows the interferometer to make images.

Very Long Baseline interferometry (VLBI) is routinely done between telescopes on different continents. Instead of having the telescopes joined by cables, the signals from each antenna can be recorded on magnetic tape and sent to the correlator, or else transported there through the internet, to be correlated.

1.1.1 Visibilities and uv coverage

When we have an interferometer, a fringe pattern is produced. We define the fringe visibility to be:

$$|V| = \frac{I_{max} - I_{min}}{I_{max} + I_{min}} = \frac{\text{Fringe Amplitude}}{\text{Average Intensity}} \tag{1.1}$$

where I_{max} and I_{min} are the maximum and minimum of the intensity pattern.

Visibilities are complex quantities: their amplitudes tell us 'how much' total emission is produced at a certain frequency; the phase tells us where it is located (how the emission is distributed). A source is resolved when the visibility goes to zero on the longest baseline [6].

An interferometer that observes a radio source in the plane of the sky (the spatial (x, y) plane) samples the visibility function in the (u, v) plane. The (u, v) plane is a complex plane that is tangent to the celestial sphere and perpendicular to the direction of the source. Each (u, v) point corresponds to the projection of a given baseline onto said plane (and hence, to a certain angular resolution in a given direction). For each baseline, the (u, v) points describe an ellipse as the Earth rotates, and hence observing a source at multiple times during the day improves the (u, v) coverage and the range of angular resolutions that are sampled.

The visibility function measured by the interferometer is given according to the van Cittert-Zernike theorem by:

$$V(u, v) = \int_{-\infty}^{\infty} \int_{-\infty}^{\infty} I(x, y) e^{i2\pi(ux+vy)} dx dy \tag{1.2}$$

$V(u, v)$ is the Fourier transform of $I(x, y)$; if the interferometer could sample *all* the (u, v) plane, then we could recover completely the brightness distribution of the source. This is not possible because the interferometer has a limited number of antennas.

Since we are only sampling the visibility function discretely, our information is limited by the number of antennas in our interferometer, their geometry (which is time-dependent), and the position of the source in the sky. In optical astronomy, the point-spread function describes

the response of an imaging system to a point source. The analogous in interferometry is the **synthesized beam**. A small numbers of antennas results in a sparse (u, v) coverage, and the side lobes of the beam become quite important.

As we increase the number of antennas the synthesized beam approaches a 2-dimensional Gaussian that can be described in terms of its full width at half maximum (FWHM) and its position angle (PA). For a given interferometric pair, the separation of the antennas as seen by the source changes as the Earth rotates (the telescopes appear to trace elliptical paths relative to each other). This allows us to measure as many Fourier components of the brightness distribution as possible per day, increasing the (u, v) coverage and smoothing the beam. This can be appreciated in figures 1.1 and 1.2 [6].

1.2 eMERLIN [2]

The Multi-Element Radio Linked Interferometer Network (MERLIN) is an interferometer array of radio telescopes spread across England which is run from Jodrell Bank Observatory (JBO) in Cheshire. The array consists of up to seven radio telescopes and includes the Lovell Telescope, Mark II, Cambridge, Defford, Knockin, Darnhall and Pickmere. The longest baseline is therefore 217 km.

eMERLIN is a major upgrade to the earlier MERLIN array. The upgrade is designed to increase the sensitivity of MERLIN by using new receivers and telescope electronics, together with an optical fibre network that connects each telescope to a new correlator at the JBO that can transport up to a bandwidth of 4 GHz. Being connected allows for the correlator to produce fringes in real time (unlike most VLBI networks, where the data has to be sent to the correlator and processed later). The telescope can currently observe in the L-band (1.23-1.74 GHz) and the C-band (4.3-7.5 GHz), in full polarization mode and with a spectral resolution ($\frac{\Delta\nu}{\nu}$) of up to 10^7 (that is, 0.03 km/s in the C-band and 0.1 km/s in the L-band). The C-band will eventually will be extended, and the K-band (22 GHz) added.

With a maximum baseline of 217 km, the angular resolution of e-MERLIN at 5 GHz is 40 mas and the field of view is 7 arcmin (the full width at half maximum of the 25 m dishes that form the array if the Lovell telescope is excluded, as is the case for our data). The sensitivity at 5 GHz can be of 2 μJy/bm in a full imaging run, although the final performance will depend on useable bandwidth and final receiver optimization. In continuum mode, for the C and K bands, the bandwidth is of 2048 MH, divided in 16 subbands of 128 MHz, each further subdivided in 512 channels of 250 kHz. The continuum bandwidth in the L-band is 512 MHz.

In the case of this work, the observations had a bandwidth of 512 MHz using four adjacent 128-MHz spectral windows. The setup made use of only 6 of the antennas, all with a diameter of 25 m; the excluded antenna is that of the 76 m Lovell telescope at JBO.

[2] Telescope information taken from e-MERLIN / VLBI National Radio Astronomy Facility [16]

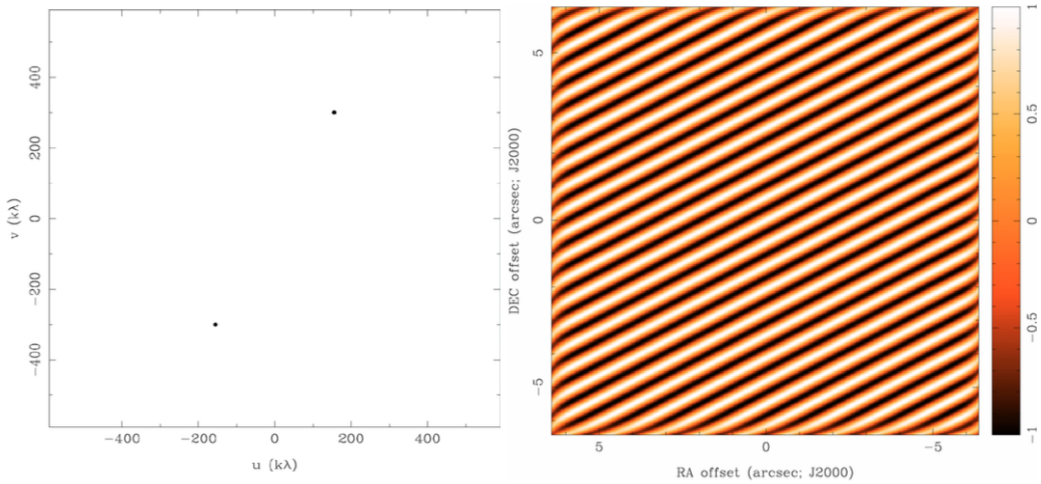

(a) Synthesized beam for two antennas

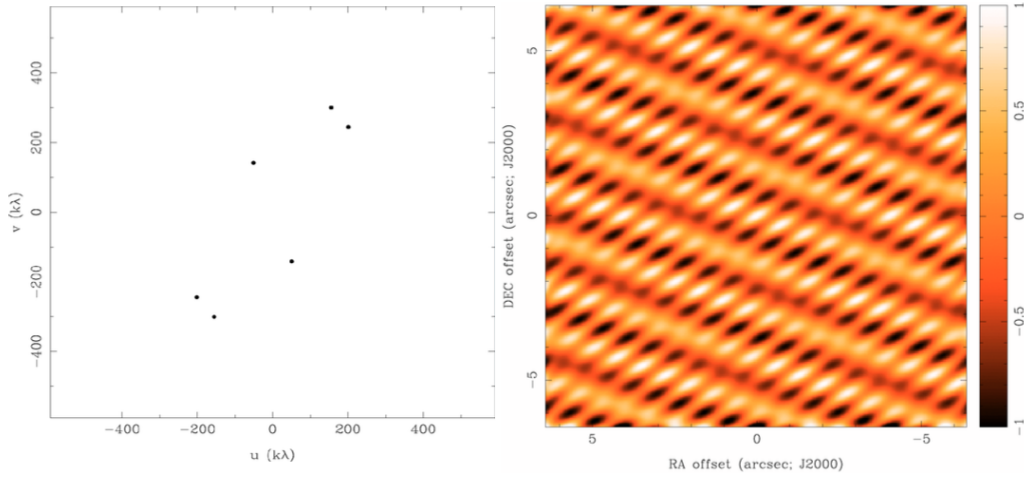

(b) Synthesized beam for three antennas

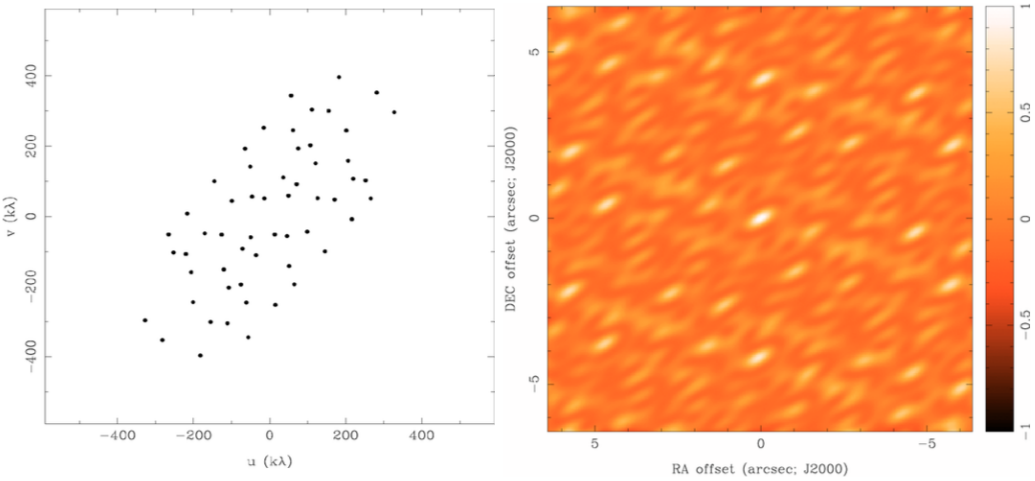

(c) Synthesized beam for eight antennas

Figure 1.1: Effects of a sparse (u, v) coverage. To the left, position of the antennas in the (u, v) plane. To the right, response of such a system to a point-source (the **synthesized beam**). Images taken from [6].

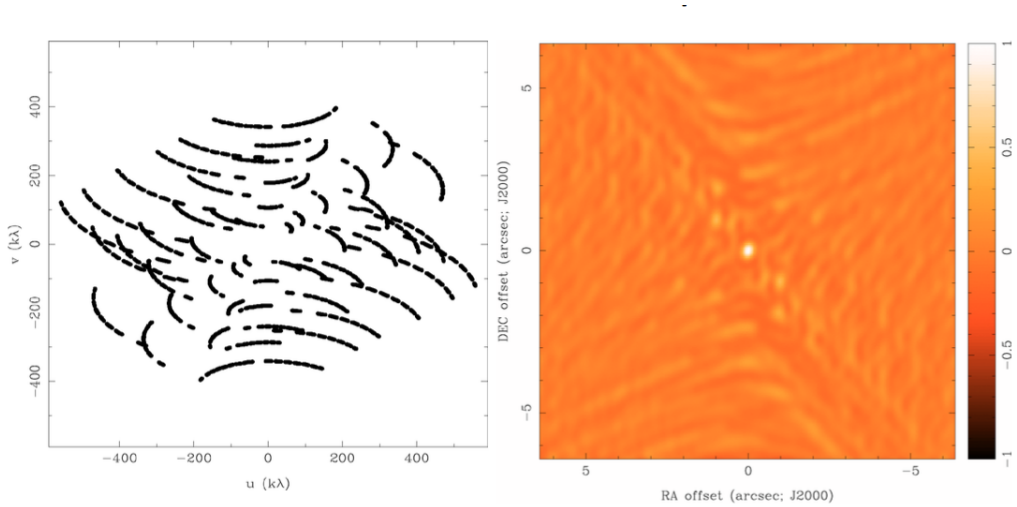

Figure 1.2: Better-sampled (u, v) plane due to Earth's rotation. The improved beam results from 8 antennas and 240 samples. Image taken from [6].

Figure 1.3: eMERLIN antennas over the map of the UK. The longest baseline is 217 km. Image from [16].

1.3 Polarization[3]

The polarization of a transverse wave is given by the orientation of the electric field vector **E**. The **E** vector can be described by a plane wave as:

$$\begin{aligned} E_x &= A_x cos(kz - \omega t)\hat{x} \\ E_y &= A_y cos(kz - \omega t + \delta)\hat{y} \end{aligned} \tag{1.3}$$

E_x and E_y propagate along the z-axis, and, for an observer looking down the direction of propagation, appear as an ellipse in the general case (if both linear and circular polarizations are present). In the case of circularly polarized radiation, the polarization plane changes; this does not happen for linearly polarized radiation.

Radio polarization is often synchrotron in origin. Synchrotron emission is non-thermal, and is produced by a charged particle in the presence of a magnetic field. It produces linear polarization, and it can vary in magnitude and position angle over the source. This work deals with synchrotron radiation, and hence the following discussion will focus on linear polarimetry.

In astronomy, the Stokes parameters are typically used to measure polarization. Of the four parameters, I is a measure of the total intensity of the wave, Q and U represent the linearly polarized component, and V represents the circularly polarized component. They completely specify the distribution of incoherent radiation from an astronomical source.

The Stokes parameters all have the dimensions of flux density or intensity, and they propagate in the same manner as the electromagnetic field. They can be determined for any point along a wave path, and their relative magnitudes define the state of polarization at that point. When they are used to specify the total radiation from any point on a source, I, which measures the total intensity, is always positive, but Q, U, and V can take both positive and negative values depending on the position angle or sense of rotation of the polarization [13].

The response of the interferometer is proportional to a linear combination of two or more Stokes parameters, where the combination is determined by the polarizations received at the antennas.

Figure 1.4 is a schematic diagram of a polarization interferometer. The incident electric field is described in terms of two components (horizontal and vertical or left- and right-circular), each of which is converted to an electric voltage by a receptor inside the feed. The receptors are sensitive to nominally opposed polarizations. Here they are labeled p and q for generality, but they are usually labeled x, y if they detect linearly polarized components or R, L for circularly polarized ones. This interferometer consists of two antennas connected to a correlator that measures the cross-correlations between a voltage from antenna A and one from antenna B. An interferometric array will be composed of N antennas, giving $N(N-1)/2$ baselines such as this one, with all four possible correlations between antenna pairs measured [12].

By observing these pairs it is possible to separate the responses of the feeds to the four Stokes parameters (which can be calculated in a simple way from radio telescope outputs) and determine the corresponding components of the visibility. The variation of each parameter over the source can thus be mapped individually, and the polarization of the radiation emitted at any point can be determined.

[3]This section borrows heavily from [10]

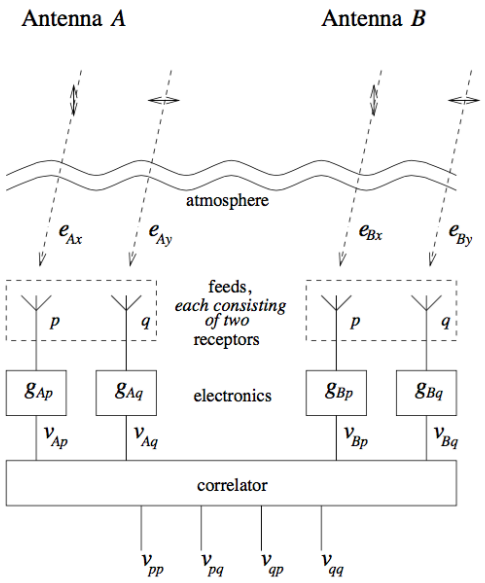

Figure 1.4: Interferometer block diagram. Taken from [12].

If $\vec{E_1}$, $\vec{E_2}$ are the electric vectors generated at the telescope aperture from the source radiation, the time average of the four possible cross-correlations of two circular feeds relate to the four Stokes parameters by:

$$\begin{aligned}
\tilde{I}_{12} &= \frac{1}{2}\left(< E_{1R}E_{2R}^{*} > + < E_{1L}E_{2L}^{*} > \right) \\
\tilde{Q}_{12} &= \frac{1}{2}\left(< E_{1L}E_{2R}^{*} > + < E_{1R}E_{2L}^{*} > \right) \\
\tilde{U}_{12} &= \frac{i}{2}\left(< E_{1L}E_{2R}^{*} > - < E_{1R}E_{2L}^{*} > \right) \\
\tilde{V}_{12} &= \frac{1}{2}\left(< E_{1R}E_{2R}^{*} > - < E_{1L}E_{2L}^{*} > \right)
\end{aligned} \tag{1.4}$$

where $\tilde{I}$, $\tilde{Q}$, $\tilde{U}$ and $\tilde{V}$ are visibilities (the Fourier transforms of the Stokes parameters), R and L refer to the (circular) polarization of the feeds, and 1 and 2 are the antennas.

The time averages are given because we are dealing with real telescope output signals. Stokes V for circular feeds is constructed by subtracting two auto-correlations from each other. In the analogous equations for linear feeds, Stokes Q is also calculated by subtracting two auto-correlations. This means subtracting two large numbers to end up with a small number, which is inherently very noisy. So linear feeds give good circular polarization measurements, and circular feeds give good linear polarization measurements [4].

The four complex cross-correlations that can be made between the signals from antennas 1 and 2 are denoted $R_1R_2^*$, $L_1L_2^*$, $R_1L_2^*$, and $L_1R_2^*$. For perfect feeds and perfectly calibrated data, these are related to the Stokes parameters by:

$$\begin{aligned} R_1 R_2^* &= \tilde{I}_{12} + \tilde{V}_{12} \\ L_1 L_2^* &= \tilde{I}_{12} - \tilde{V}_{12} \\ R_1 L_2^* &= \tilde{Q}_{12} + i\tilde{U}_{12} \\ L_1 R_2^* &= \tilde{Q}_{12} - i\tilde{U}_{12} \end{aligned} \tag{1.5}$$

From these equations it follows that the total intensity distribution is the Fourier transform of the average of the RR and LL correlations, and that the linear polarization is obtained from the Fourier transform of combinations of the cross-correlations. The cross-hand fringes typically have small amplitudes, so large antennas and wide bandwidths are required for polarization experiments.

In practice, the characteristics of the antennas can cause an unpolarized source to appear polarized. This is the so-called *instrumental polarization*. The voltage induced in each antenna is the sum of a term which is the response of the feed to its nominal polarization, and a second term which is the response of the feed to orthogonally polarized radiation due to imperfections of the feed. In addition, each chain has an overall, complex multiplicative gain, due to the conversion of the voltages detected in individual chains to complex visibilities in units of flux density in each baseline. For circular feeds

$$\begin{aligned} V_R &= G_R(E_R e^{-i\phi} + D_R E_L e^{+i\phi}) \\ V_L &= G_L(E_L e^{+i\phi} + D_L E_R e^{-i\phi}) \end{aligned} \tag{1.6}$$

G_R and G_L are time-dependent gain factors associated with each channel, with amplitude g and phase ψ:

$$G_{1R}(t) = g_{1R}(t) e^{i\psi_{1R}(t)} \tag{1.7}$$

D_R and D_L are the responses of each feed to radiation of incorrect polarization and are referred to as *leakage* parameters, and ϕ is the parallactic angle of the source (the orientation of the sky in the telescope's field-of-view).

The variation in ϕ between different observations of a calibration source permits the $D-$terms to be separated from each other and from the source polarization. Hence, a good parallactic angle coverage is required to do interferometric polarization.

Including gains and $D-$terms in equations (1.5), dropping second-order terms, and considering that $\tilde{V}$ has a negligible effect (as it does for radioastronomical sources with non-thermal radiation at centimeter wavelengths), we obtain the following equations:

$$\begin{aligned} R_1 R_2^* &= G_{1R} G_{2R} \tilde{I}_{12} e^{i(-\phi_1+\phi_2)} \\ L_1 L_2^* &= G_{1L} G_{2L}^* \tilde{I}_{12} e^{i(+\phi_1-\phi_2)} \end{aligned} \tag{1.8}$$

$$\begin{aligned} R_1 L_2^* &= G_{1R} G_{2L}^* [\tilde{P}_{12} e^{i(-\phi_1-\phi_2)} + D_{1R} \tilde{I}_{12} e^{i(+\phi_1-\phi_2)} + D_{2L}^* \tilde{I}_{12} e^{i(-\phi_1+\phi_2)}] \\ L_1 R_2^* &= G_{1L} G_{2R}^* [\tilde{P}_{21}^* e^{i(+\phi_1+\phi_2)} + D_{1L} \tilde{I}_{12} e^{i(-\phi_1+\phi_2)} + D_{2R}^* \tilde{I}_{12} e^{i(+\phi_1-\phi_2)}] \end{aligned} \tag{1.9}$$

Here, $\tilde{P} = \tilde{Q} + i\tilde{U}$

In the cross-polarization response the contamination terms have order one, and so it is important that the contamination terms are well calibrated for polarimetric observations. For a pair of antennas, knowing the leakage terms allow us to express the measured correlator outputs in terms of the corresponding correlations as they would be measured with ideally polarized antennas.

In a typical polarization experiment, we chose a polarization calibrator that is bright (so that the fringes have high signal-to-noise) and that has little or no polarization (so that the $D-$terms dominate). 1407+284 (OQ 208) fulfills these conditions at 5 GHz, and is the calibrator used in this work.

A drawback of this treatment is that the absolute orientation of the polarization vectors is lost. Thus, a good polarization angle calibrator is also needed. 1331+305 (3C286) is a good option, and is the one used in this work [4].

The principal difficulty in interferometric polarimetry is that the instrumentally induced polarization signals are of the order of the true polarization signal from the source.

1.4 Analysis of an interferometry experiment: data reduction

After a radio observation, the data-streams are either recorded in tapes and mailed to the correlator, sent through the internet, or, as in the case of eMERLIN, sent through optical fibre. In interferometry the signals arrive at each antenna with a delay with respect to a reference antenna. The correlator, for each baseline, aligns the tapes temporally and in frequency, reads and decodes the data, aligns the data sequences for each station compensating for an *a priori* delay τ_0 (which corresponds to the clock difference between stations and the geometric signal delay); multiplies each pair of sequences within a range of delay values τ and fringe rates $\dot{\tau}$ around τ_0 generating a correlation function; and stores the results. Then the correlator looks for the maximum of the correlation function [8].

Once the signal from the antennas is collected, amplified, converted, transported, correlated and averaged, the data from each antenna pair are recorded. These are referred to as the *observed* visibility data. The purpose of a calibration is to recover the *true* visibility, the Fourier transform of the source's brightness distribution.

In order to illustrate the calibration process, I will use data taken with the e-MERLIN interferometer and analyzed with the Astronomical Image Processing System (`AIPS`) package. The sources will be discussed in more detail further on in this work. I will also mention the `AIPS` tasks required to perform each calibration step. These are summarized in table 1.2.

In this case, the data consists of the following sources:

- 1407+284: an unpolarized source, which allows us to determine the D-terms;
- 1331+305: amplitude calibrator, which allows us to determine the absolute orientation of the polarization angle;
- J1933+6540: the phase calibrator. This is a strong compact source to look for the interferometric observables, that are later transferred to the target;

- B1938+6648: the target.

The data are taken with six e-MERLIN antennas, labeled 2, 5, 6, 7, 8, and 9 (alternatively, MK2, KN, DE, PI, DA, and CM). The bandwith is 512 MHz divided in four subbands or intermediate frequencies (IF), which are electronically independent, have a bandwidth of 128 MHz, and are further subdivided in 512 channels of 0.25 MHz.

1.4.1 Data editing and flagging

The first step in a calibration is to examine the data, and to discard discrepant and severely corrupted data (the outliers). The task `LISTR` lists all observations in a file, including the exact times in which the antennas are pointed towards a source. It is necessary to be clear on the time intervals in which our data are corrupted, because that information will be included in the flagging step. `LISTR` also provides parallactic angle information. We need to make sure that the polarization calibrator is observed with a range of parallactic angles so that our $D-$term solutions later on are not degenerate.

To examine the data we can use the task `POSSM`. `POSSM` plots, for a specified baseline and integration time, the total and cross-power spectra of a source. It gives us information on both the phases (upper part of the diagram) and the amplitudes (lower part of the diagram). It allows us to identify very obvious radio frequency interference (RFI, which can look like spectral lines), or time periods when an antenna is not pointed towards the source. Fig. 1.5 illustrates the role of this task.

`SPFLG` plots, for each channel and for each scan, the visibility of the correlations or Stokes parameters of our choice. In `SPFLG` we can detect RFI, which is visible as vertical strip that corresponds to one or a few channels (i.e., to a narrow band of frequencies). This strip has a much higher intensity than the surrounding data points. `SPFLG` allows us to manually flag data points that do not correspond to the source and hamper the data reduction (see fig. 1.6). Apart from RFI and off-source antennas, it is useful to flag the first and last few channels of each IF (intermediate frequency, or subband) where, as can be seen in fig. 1.5, detect lower intensities than the central, more reliable, band.

1.4.2 Bandpass calibration and fringe-fitting

In certain cases, the antenna gains G_i might not be constant over the bandwidth. To handle changes of antenna gain with channel, we can consider that the baseline-based gain as a function of frequency $G_{ij}(\nu)$. Compensating for the change of gain with frequency is called **bandpass calibration** [3]. It is done with `AIPS` task `BPASS`, which creates a table that contains the bandpass response functions of the antennas. Because of the narrow channel widths, accurate calibration of the antenna badpasses should only be done using very strong calibrators that give high signal-to-noise even for very small bandwidths (here, 1331+305). The time variation of bandpass functions is usually slow, so a single calibration per observing run is sufficient. Applying `BPASS` has the effect of aligning the phases in the `POSSM` plot, as seen in fig. 1.7.

In Very Long Baseline Interferometry it is necessary to carry out a fundamental step called **fringe-fitting** or **delay calibration**. As mentioned before, the correlator correlates the data compensating for a range of delay values τ around τ_0. The *a priori* delay τ_0 calculated from geometric models

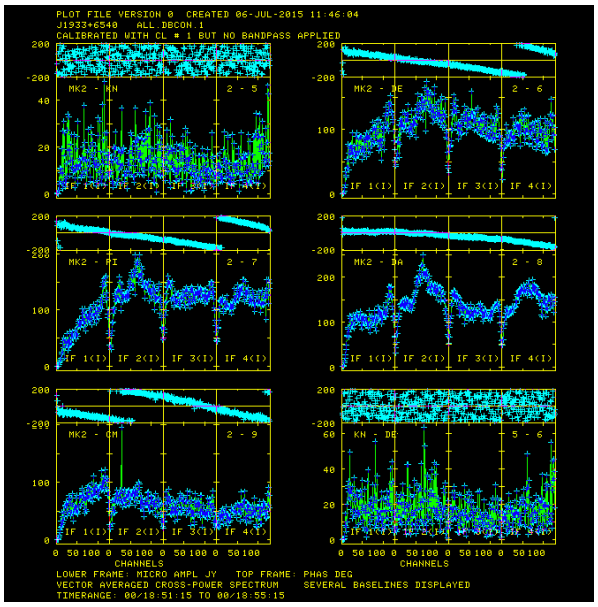

Figure 1.5: `POSSM` plot of amplitudes and phases as a function of channel for source J1933+6540 and for baselines 2-5, 2-6, 2-7, 2-8, 2-9, and 5-6. Integration time is 4 minutes. Notice that for this time range antenna 5 is not on source (plots 1 and 6, which show only noise). In plot 5, which corresponds to baseline 2-9, there is a big interference spike in the second IF.

and propagation media estimates is subject to errors, which causes drifts in the interferometric phase in time and frequency. These are additional contributions to the delay originating from the atmosphere and the instrumentation. These drifts are eliminated by fringe-fitting [8].

In a grid of combinations of $(\tau, \dot{\tau})$, the correlation of signals between antennas is maximum for a pair $(\tau_\phi, \dot{\tau_\phi})$, where τ_ϕ is the delay value, which depends on the specific physical conditions (interferometer geometry, source position, atmosphere, different path lengths in each antenna, etc), and $\dot{\tau_\phi}$ is its time derivative, the delay rate. These quantities are defined as:

$$\begin{aligned} \phi &= 2\pi\nu\tau_\phi \\ \dot{\tau_\phi} &= \frac{1}{2\pi\nu}\frac{\partial\phi}{\partial t} \end{aligned} \tag{1.10}$$

If we consider all the channels, the slope of the linear fit of the phase delay per channel defines the group delay:

$$\tau_G = \frac{1}{2\pi}\frac{\partial\phi}{\partial\nu} \tag{1.11}$$

So overall the interferometric phase has a series of additive contributions (geometric, atmospheric, instrumental, and due to the extended structure of the radio source):

$$\phi = \phi_{geo} + \phi_{atm} + \phi_{instr} + \phi_{strc} + 2\pi n \tag{1.12}$$

The `AIPS` task `FRING` determines the group delay and phase rate calibration to be applied to the data set given a model of the source. This is done for the calibrators, which can be considered a compact source for each individual scan.

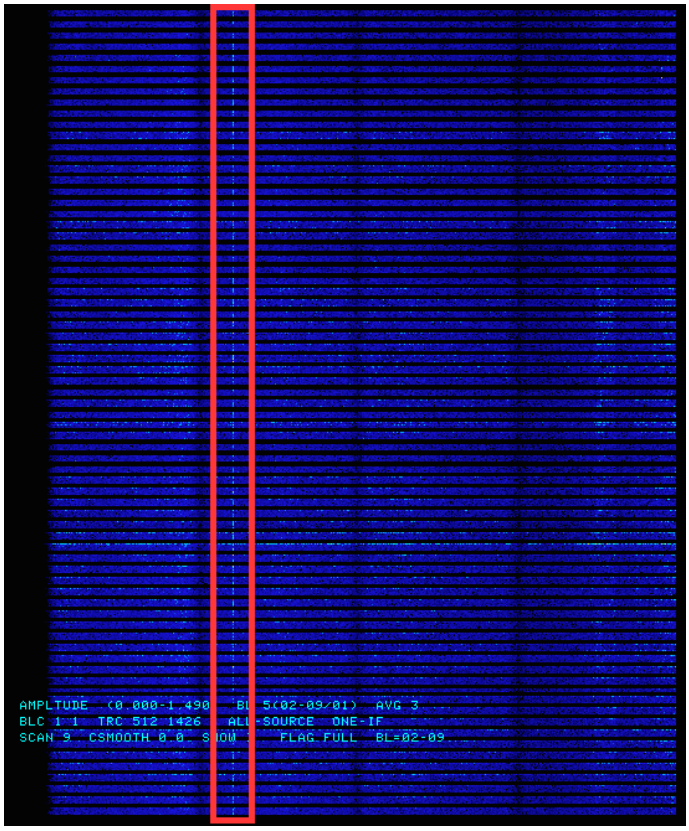

Figure 1.6: `SPFLG` plot of J1933+6540 displaying Stokes I for baseline 2-9. On the x-axis are the channels and on the y-axis is time (each horizontal line corresponds to a scan), and intensity is color-coded. In this figure, the second IF displays a thin RFI line (inside the red box), which is the same interference as that from figure 1.5 present in antenna 9. It shows an extremely large value for the amplitude.

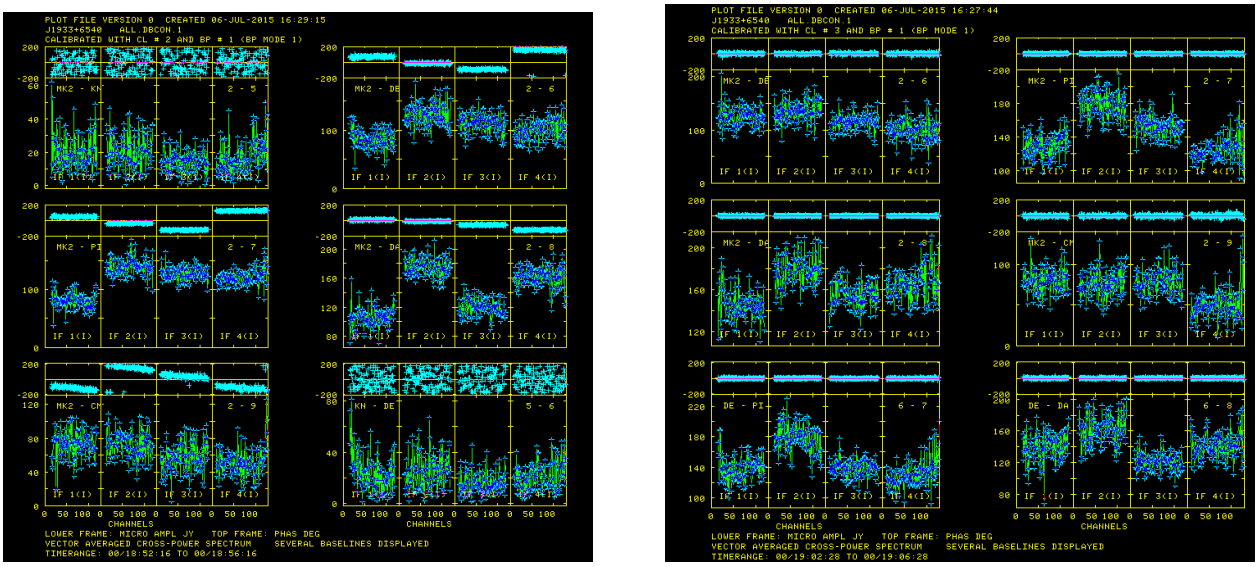

Figure 1.7: **(a)** `POSSM` plot of J1933+6540 (same scan as in fig. 1.5) after calibrating for the bandpass. Note that, for each IF, the frequencies are aligned. **(b)** `POSSM` plot of J1933+6540 after finge-fitting. Now all IF phases are aligned and the four IFs behave line a single interferometer.

IF	1	2	3	4
Central freqs.	5.2453 GHz	5.3733 GHz	5.5013 GHz	5.6293 GHz
1407+284	2.76277 ± 0.36193	2.75670 ± 0.37398	2.69477 ± 0.33318	2.67329 ± 0.35546
J1933+6540	0.55644 ± 0.03127	0.57981 ± 0.04126	0.58189 ± 0.05298	0.63944 ± 0.07623

Table 1.1: Flux densities in Jy/bm of 1407+284 and J1933+6540.

By aligning the phases in frequency and time we make all four IFs behave as a single interferometer of 512 MHz bandwidth, instead of as four different interferometers of 128 MHz each, and hence we increase the equivalent bandwidth. Since

$$SNR \propto \frac{1}{\sqrt{(BW)}\sqrt{(\Delta \mathrm{t})}} f(\mathrm{g}, \mathrm{atm}, ...) \tag{1.13}$$

(where BW is the bandwidth, Δt the integration time, and f is a function of instrumental and atmospheric factors), an increase in bandwidth improves the signal-to-noise.

1.4.3 Amplitude calibration

The process of converting the correlation amplitude (in arbitrary units) to flux density (in Janskys) is called 'amplitude calibration.' To calibrate in amplitude we use compact and bright radio sources with a known flux density. In this case, the calibrator is 1331+305. At centimeter wavelengths, the use of standard gain curves and frequent measurements of system temperatures fix the amplitude scale to within 10% [10]. Finer adjustment of the relative amplitude gains of the antennas can be made in the self-calibration step.

We use a flux calibrator whose behaviour at a given frequency is well-known. The task `SETJY` allows us to introduce the model for 1331+305 alongside our data (i.e., we fix the flux density values our observations should have, taking into account the structure of the source at each wavelength). By comparing the model to our observations with task `CALIB`, we solve for the antenna gains, and we know what corrections we need to apply to the remaining sources to recover their flux densities.

We run `CALIB` (based on the gains determined for 1331+305) with 1407+284, assuming it's a point-source, and then the task `GETJY` lists the recovered flux density per IF. Next, we run `CALIB`, this time for J1933+6540 (the phase calibrator of our target) and using 1407+284 as a reference, and again `GETJY` gives us J1933+6540's flux density values. These are all listed in table 1.1, and the effect of the calibration can be appreciated in fig. 1.8.

`AIPS` stores all these corrections in calibration tables. These tables can be layered, and we need to chose, each time, what calibration table we want to use on our data. Since it can get confusing to keep track of what table carries which corrections to what source, and since it is difficult for `AIPS` to handle the whole (large) data set each time we perform a task, we use the task `SPLIT` to separate the file containing all tables and all sources into individual source files. We split the data set in such a way that the smaller files have the editing, bandpass, delay, and amplitude calibrations already applied.

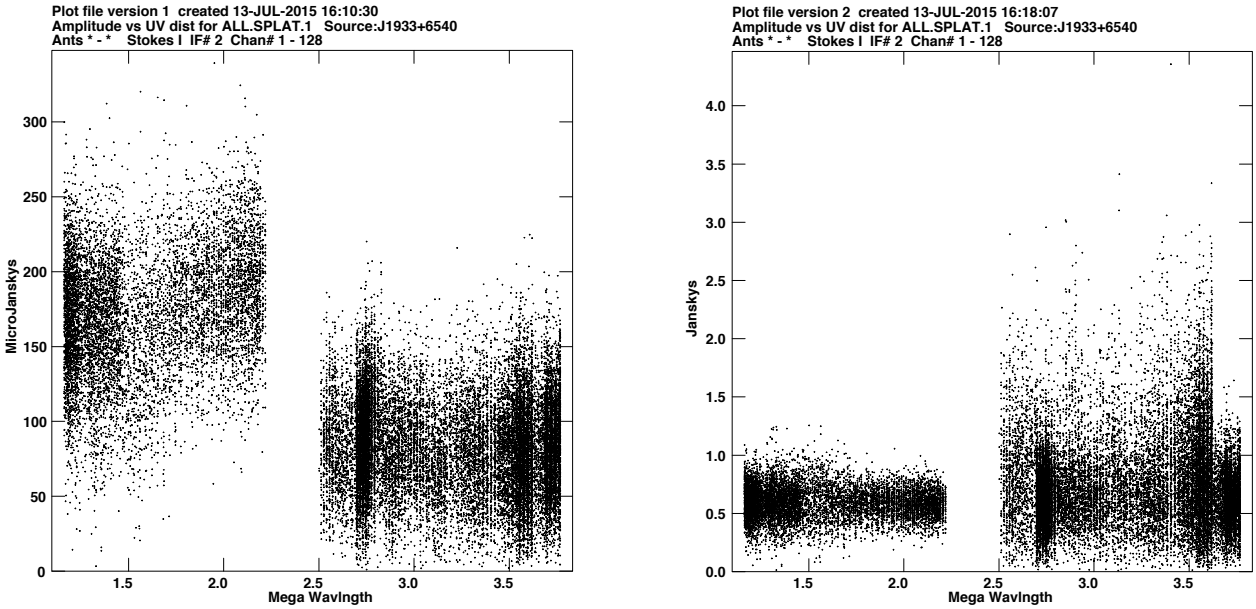

Figure 1.8: (a) `UVPLT` plot of J1933+6540 with observed visibilities in IF2 (Stokes I) as a function of distance between the antennas, in wavelengths. **(b)** Same `UVPLT` plot of J1933+6540 *after* the amplitude calibration. The large scatter of the longest baselines corresponds to the small SNR. Integrating in time and bandwidth, the scatter is reduced. The data shown are for an integration time of 2 seconds and individual frequency channels.

1.4.4 Self-calibration, cleaning, and imaging

The method employed for the data calibration is known as **self-calibration**. Amplitudes and phases provide information on the source structure, but they are affected by the gain errors in each antenna. The gain correction we have done previously is not good enough, since the gains are calculated for a different time than the observation of the target (i.e., when we observe the calibrator at the beginning and the end of the observing session), and in a different direction (that of the calibrator, not that of the target). The gains depend on the atmosphere (which can be variable in the timescale of an observation, and is certainly different according to what position in the sky the telescope is pointing at) and the electronics (which can also vary within an observation). In order to distinguish between source components and gain errors we assume a brightness distribution in the source, and calculate theoretical visibilities without gain errors. We then measure the differences between observed and model visibilities and find gain values that can minimize said difference [3].

This is to say: for a baseline $i-j$, where m stands for measured, t stands for true, $G = |G|e^{i\psi}$ are the complex gains, and ϵ is white noise, we have that the measured visibility is:

$$V_{ij}^{m}(u,v) = G_i G_j^{*} V_{ij}^{t}(u,v) + \epsilon_{ij} \tag{1.14}$$

which we can also write as

$$|V_{ij}^{m}|e^{i\phi_{ij}^{m}} = |G_i||G_j|e^{i(\psi_i-\psi_j)}|V_{ij}^{t}|e^{i\phi_{ij}^{t}} + \epsilon_{ij} \tag{1.15}$$

(Here, $V^t(u,v)$ is the Fourier transform of the real source's intensity distribution $I(x,y)$.)

What the self-calibration does is that it takes an image of the source ($I_1(x,y)$), which we assume to be true, and solves (using least squares) for G_i, G_j. We can apply these gains to

correct the observed data, which we can use to create a new and improved model for the corrected data (a second iteration $I_2(x, y)$). We continue supplying new images that we consider 'true' and solving iteratively (initially for the phases, later for the amplitudes as well) until we arrive at a satisfactory image. This is done with the task `CALIB`, where the inputs are the image with which we self-calibrate, and the (u, v) data points of the source file *after* `SPLIT`[4] (we always self-calibrate with the same file, else we would be calibrating on an image that has already been calibrated). We can set `CALIB` to solve for the phases of the gains or for both the phases and the amplitudes. We also give `CALIB` a minimum number of baselines for which solutions must be found.

The way to supply at each step a more reliable image from which to start the self-calibration process (including the first one) is through the **cleaning** algorithm.

The first image is produced the following way: we take the Fourier Transform of the measured visibilities $V^m(u, v)$ and obtain the first dirty map $I^D(x, y)$. Cleaning is done to that map, and the remaining map is our first iteration image $I^1(x, y)$:

$$V^m(u, v) \xrightarrow{\text{FT}} I^D(x, y) \xrightarrow{\text{CLEAN}} I^1(x, y) \tag{1.16}$$

Cleaning works to deconvolve the beam (which can have big side lobes due to incomplete (u, v) coverage) from our *dirty* map I^D to obtain the *clean map* I^C, the end goal of our imaging. It assumes that our image consists of a number of point sources, locates the maximum in the dirty map and subtracts the instrumental response to a point-source in that location. It follows these steps [8]:

1. It finds the peak brightness in the dirty map I^D.

2. It subtracts from the dirty map the effect of the synthesized beam (see fig. 1.9) from a point source with the position and brightness of the previously found maximum, multiplied by a gain that we set (in this case a gain of 0.1).

3. In the remaining map (the *residual map*), it locates the peak brightness and repeats step 2.

4. It continues until the residual peak is below a specified level.

5. It convolves the model of extracted point sources with an idealized beam (the *clean beam*) so that our remaining map is not just a sum of delta functions. This clean map is the central part of the dirty beam, free of the secondary lobes.

6. It adds the residuals that remain from the dirty map to the map from step 4.

This is how we obtain the clean map I^C, which is what we later use as the self-calibration model from which to find the gains. Here we have used the `AIPS` task `IMAGR` to clean.

Cleaning and self-calibration can be alternated iteratively until the obtained structure converges to the real brightness distribution. See figures 1.10 and 1.11 to visualize the effect of these data reduction steps.

[4]Which was already calibrated for bandpass, delay and amplitude.

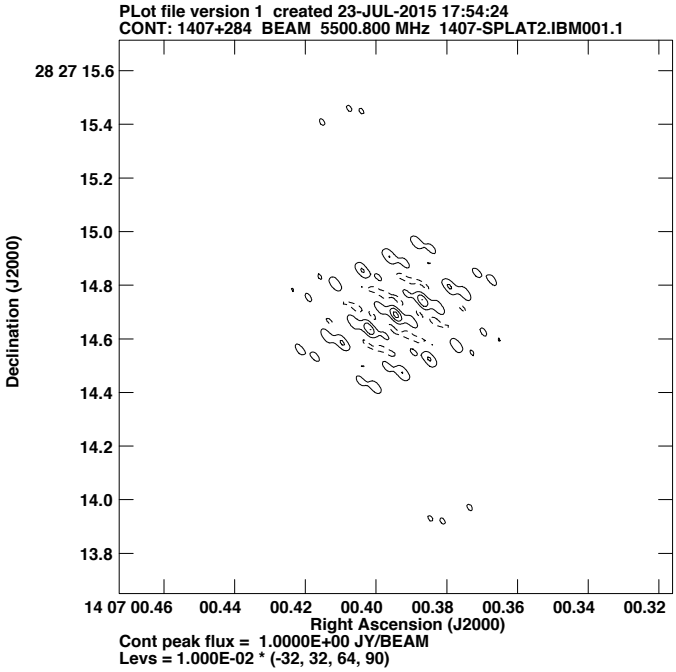

Figure 1.9: Beam that `IMAGR` subtracts when cleaning 1407+284. The beam is, of course, independent of the source, but it depends on the (u, v) coverage, that is specific to a time of the day, and hence to the observations of a particular source. Note that there are secondary lobes *up to a level of 64% the maximum.*

1.4.5 Polarization calibration and imaging

As discussed earlier, the fractional polarization of almost all astronomical sources is of the order of the leakage and gain terms that define the instrumental polarization. Therefore, to obtain a reliable measurement of the polarization of a source, the leakage and gain terms need to be accurately calibrated. Gains have been determined in the earlier calibration steps; in this section we will deal with the determination of the D-terms.

Since the two circular polarizations are detected with separate electronics, the delays in an interferometer are polarization-dependent. We use the `AIPS` task `RLDLY` to determine the group delay difference between the R and the L polarizations using observations of RL and LR correlations. That is to say, `RLDLY` corrects the delays on the cross-hands, which manifest themselves as phase slopes across the bandpass on the LR and RL correlations. The source should have a significant flux in the cross polarizations so that the phase slopes may be discerned. These come from a real Q and U signal from a polarized source such as 1331+305 (the one used in this work). `RLDLY` is a special version of fringe-fitting.

Once we have accounted for the RL delay, we compute the polarization corrections (the $D-$terms). To do this, we look at the polarization values of our unpolarized calibrator, 1407+284. Since the source is unpolarized, any polarization must be due to the instrumental contribution. See fig. 1.12 **(a)** to see the polarization signal read out without calibration.

Polarization calibration is done with task `PCAL`. `PCAL` reads a UV file, calibrates, subtracts a model and determines the effective feed parameters for each antenna and IF. These parameters are

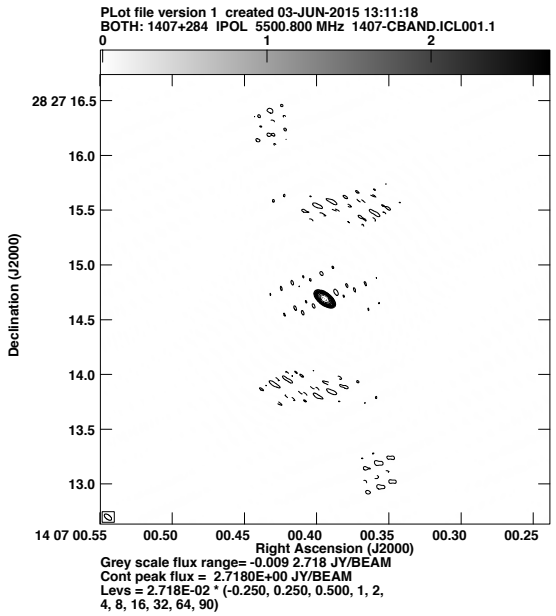

(a) 1407+284 with no self-calibration. rms = 2.11×10^{-3} Jy/bm.

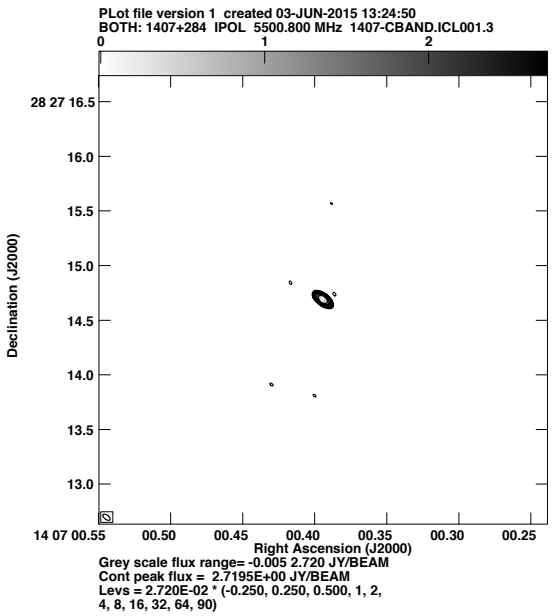

(b) 1407+284 with self-calibration in amplitude and phase. rms = 1.05×10^{-3} Jy/bm.

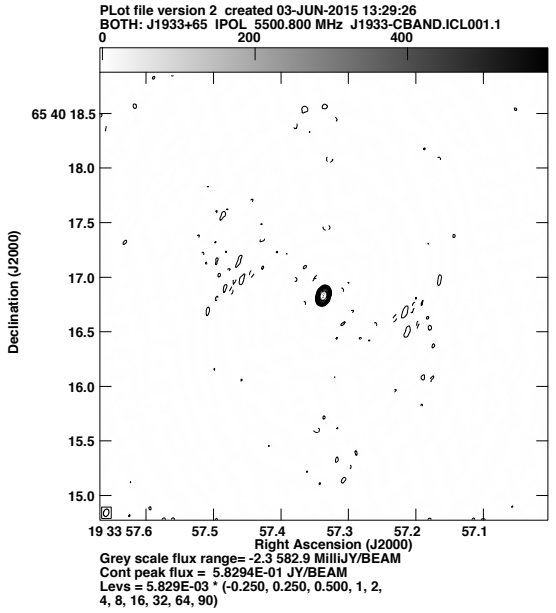

(c) J1933+6540 with no self-calibration. rms = 5.27×10^{-4} Jy/bm.

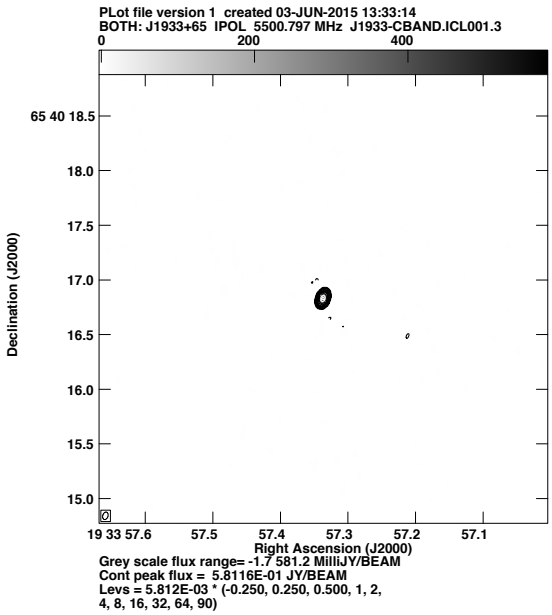

(d) J1933+6540 with self-calibration in amplitude and phase. rms = 2.82×10^{-4} Jy/bm.

Figure 1.10: Effect of self-calibration and cleaning on the calibrators. All figures have the same percentage contour levels drawn, but note that the beam effects are significantly reduced for maps on the right. Between each self-calibration, a cleaning of 2000 iterations is performed.

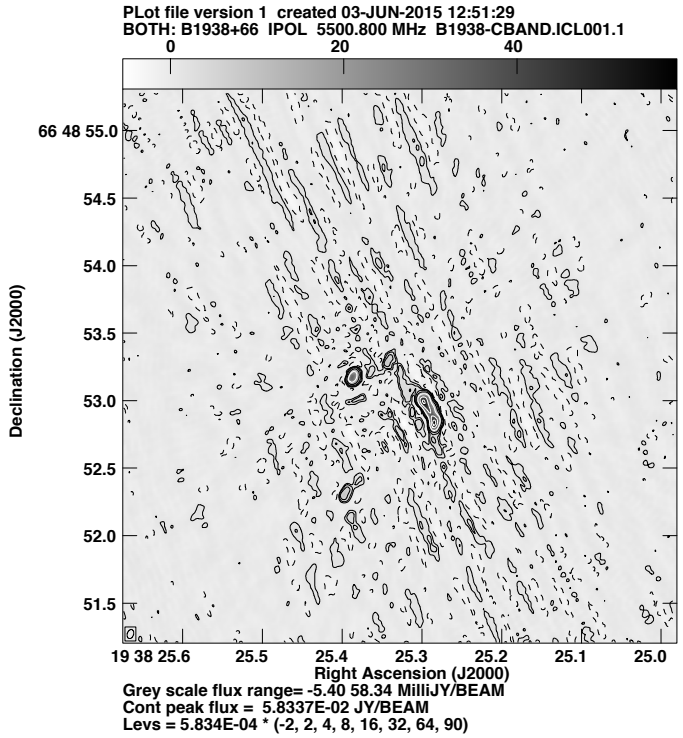

(a) The target source B1938+6648 with no self-calibration, rms = 8.09×10^{-4} Jy/bm.

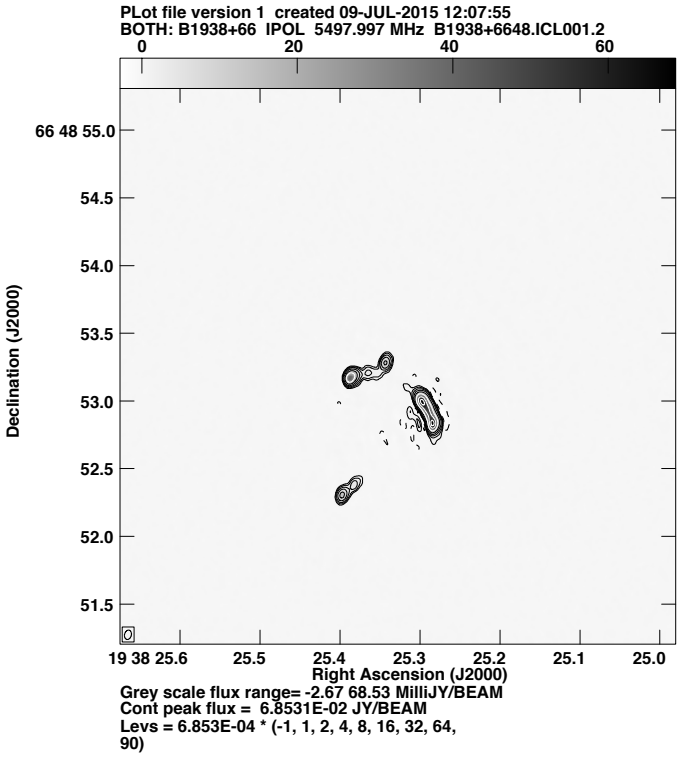

(b) B1938+6648 with 5 self-calibrations in phase and one in amplitude and phase, rms = 1.02×10^{-4} Jy/bm.

Figure 1.11: Effect of self-calibration and cleaning on the target. Note that plotted contours are *lower* in the clean image. Since it is a complex structure, the self-calibration is very important.

then placed in a table that can be applied when required. The dramatic effect of applying PCAL can be seen in figure 1.12.

PCAL has two modes. In the first mode, it averages spectral channels and determines antenna $D-$terms on a per IF basis. In the second mode, PCAL determines the $D-$terms on a per spectral channel basis. In this work we have calculated the $D-$terms both ways (integrating an IF bandwidth and finding a common $D-$term value, or finding the $D-$terms separately for each channel), and later in this section I will discuss which way gives better results for eMERLIN data. When the bandwidth is very large, the correction along the whole bandwidth cannot be accurate enough.

The last step in the calibration consists of setting the absolute orientation angle of polarization. This is done with RLDIF, which rotates the polarization angle of 1331+305 to match its known value (33°). This correction is then applied to the remaining sources before imaging, so that their polarization angles have the correct orientation as well. Fig. 1.13 displays this last correction.

Q and U are visibilities that can be Fourier transformed, and so we can obtain polarization images. Cleaning can also be done with IMAGR for Q and U dirty maps to obtain Q and U clean maps. The corresponding polarization images are made using the antenna gains $G(t)$ that are automatically found along with the I images in the hybrid-mapping procedure. In this case we did one additional amplitude and phase self-calibration for each source. Polarization images can be represented through combinations (via the task COMB) of the Stokes parameters Q and U to obtain physically meaningful quantities: the total polarization intensity $\sqrt{U^2+Q^2}$, and the polarization angle $\arctan\frac{Q}{U}$.

1.5 The *D*-terms

A current aim in interferometry studies is to improve the sensitivity these instruments can reach. As can be seen from equation (1.13), one way to achieve this is to increase the bandwidth. Thanks to recent updates, there are several radio interferometers, including eMERLIN, that are able to observe with very wide bandwidths (512 MHz, in eMERLIN's case). The European VLBI Network (EVN) can use bandwidth of up to 2 GHz. It will be even better in the case of the Square Kilometer Array (SKA) in the future.

As the bandwidth increases, integrating along the entire bandwidth becomes more problematic, since many contamination features are frequency-dependent (such as the effect of the atmosphere). This is the case for the instrumental polarization parameters. In this section we explore the effect of frequency on the leakage terms for eMERLIN: whether we can consider a common, averaged $D-$term per IF, or whether we should solve for the $D-$terms individually per channel. We conclude that solving for the $D-$terms individually per channel gives a much better polarization correction, and therefore a better determination of the polarization of the target source.

Table 1.3 summarizes the peak polarization and noise values for two calibrators for integrated bandwith and single channel polarization corrections.

The first row corresponds to peak polarization and rms values of the zero-polarization calibrator, with polarization corrected for each IF globally (that is to say, four $D-$terms for the entire bandwith) and with polarization corrected for each channel (2048 $D-$terms for the entire

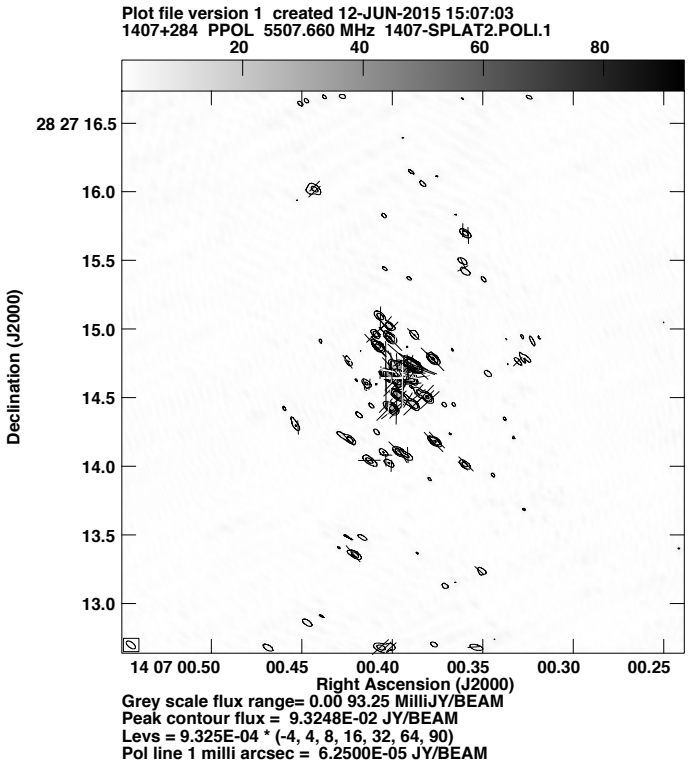

(a) 1407+284 before polarization calibration. rms $= 5.64 \times 10^{-4}$ Jy/bm.

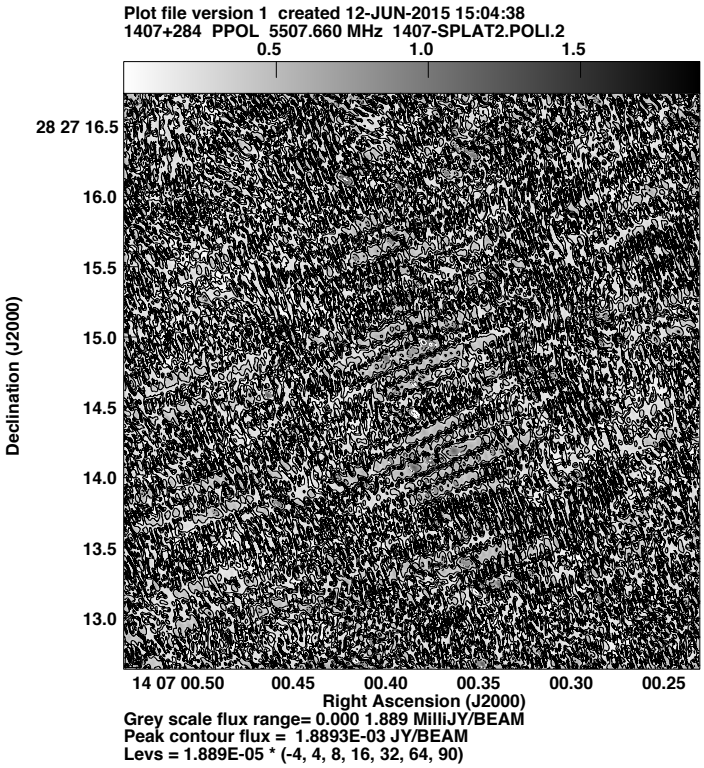

(b) 1407+284 after polarization calibration. rms $= 1.31 \times 10^{-4}$ Jy/bm.

Figure 1.12: Effect of polarization calibration. All polarization signal in **(a)** is spurious. In the corrected image there is no signal, everything is noise. The maximum has been reduced from 93.25 mJy/bm to 1.89 mJy/bm. The peak was instrumental.

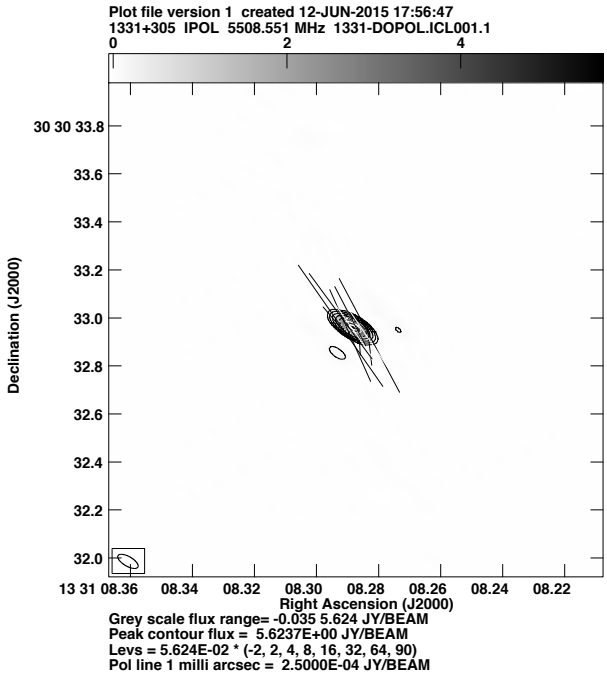

Figure 1.13: 1331+305 after entire polarization calibration. 1331+305's absolute orientation angle is 33°. Angles are measured counter-clockwise and down from the horizontal. This rotation of the polarization vectors is applied for all the sources.

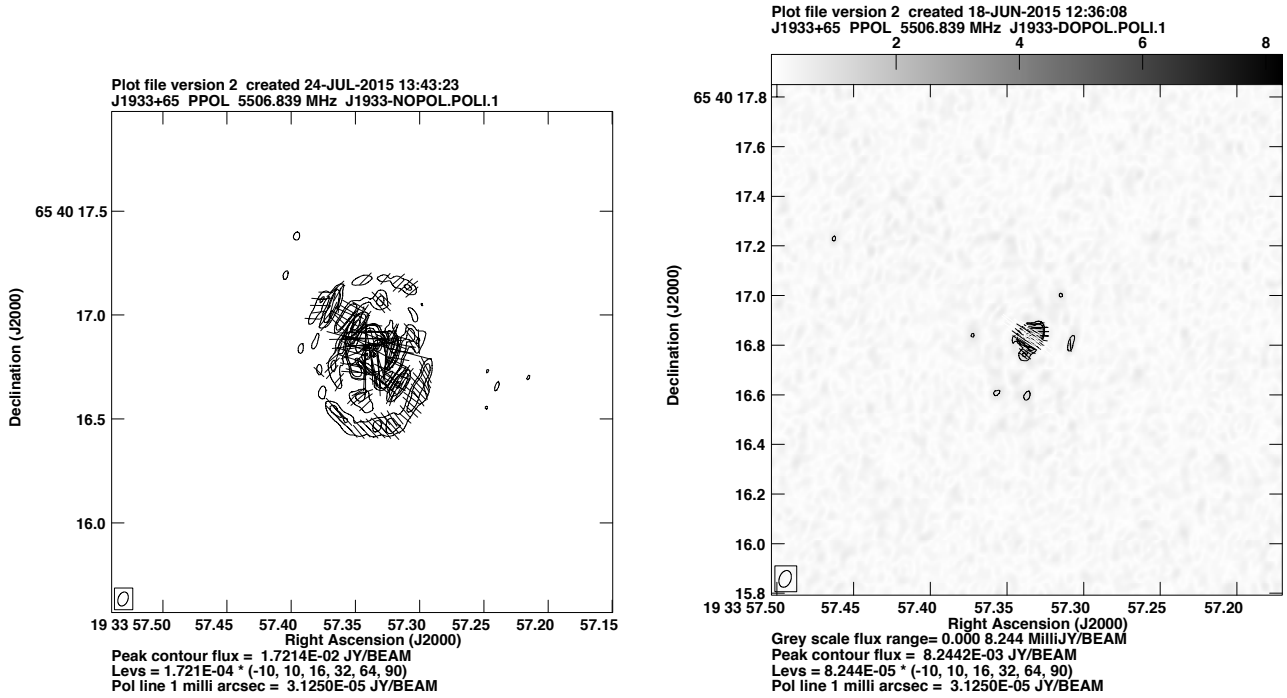

Figure 1.14: J1933+6540 (phase calibrator) without and with polarization calibration. For left figure, the instrumental polarization displayed in figure 1.12(a) is convolved with the source to produce this image. For the right figure, calibration is done in single channel mode; rms = 115 μJy/bm.

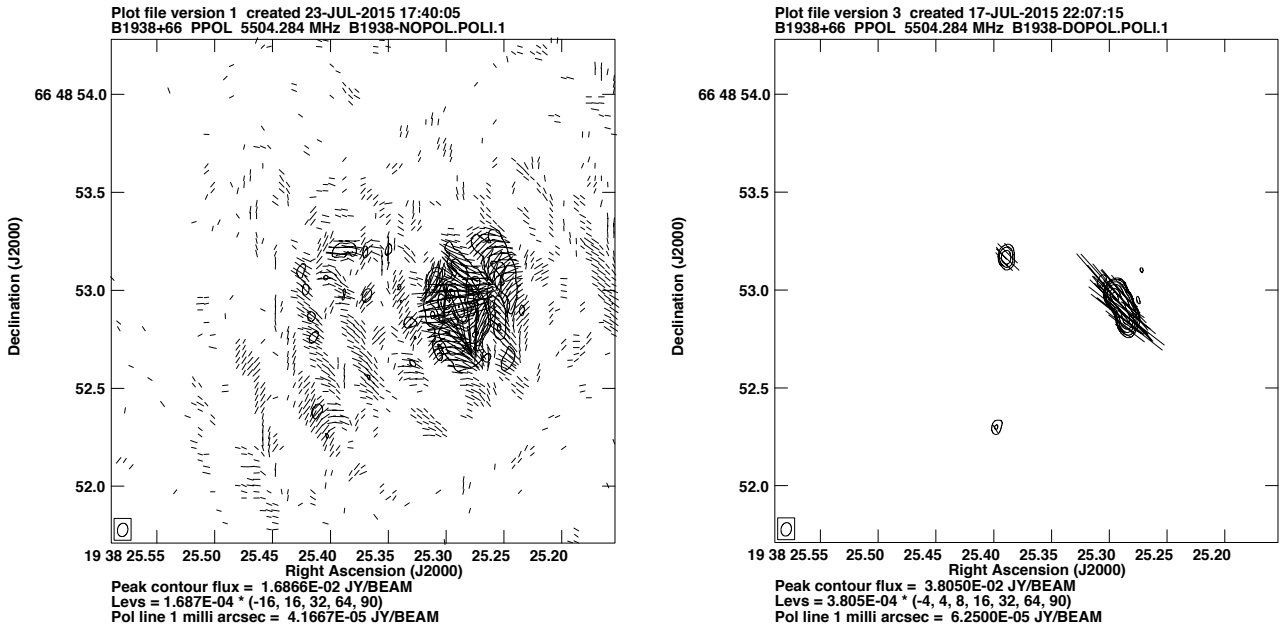

Figure 1.15: B1938+6648 (target) without and with polarization calibration. For left figure, the instrumental polarization displayed in figure 1.12(a) is convolved with the source to produce this image. For the right figure, calibration is done in single channel mode.

Calibration step	`AIPS` **task**	**Comments**
	`FITLD`	Loads .fits files from correlator
Examining the data	`LISTR`	Lists observations
	`POSSM`	Amp & phase per channel
Flagging	`SPFLG`	Spectral flagging; looking for RFIs
Bandpass calibration	`BPASS`	1331+305; then with J1933+6540
Fringe fitting	`FRING`	1331+305, 1407+286; then J1933+6540
Amplitude Calibration	`SETJY`	1331+305 Model
	`CALIB`	1331+305, 1407+284, J1933+6540
	`GETJY`	1407+284, J1933+6540
	`SPLIT`	Splits file into individual source files
Self-calibration	`CALIB`	Several iterations in
	`IMAGR`	phase and amp per source
Polarization calibration	`RLDLY`	RL phase difference (1331+305)
	`PCAL`	Determines the D-terms (1407+284)
	`RLDIF`	Absolute orientation of pol. angle (1331+305)
Imaging	`KNTR`	Contour plots in intensity
	`COMB`	Combines Q and U for intensity and angle
	`PCNTR`	Contour and vector plots for polarization

Table 1.2: Summary of data reduction steps.

Source	global IFs		single channels	
	pol peak	rms	pol peak	rms
1407+284	5.52 mJy/bm	455 μJy/bm	1.89 mJy/bm	139 μJy/bm
1331+305	618 mJy/bm	1.03 mJy/bm	662 mJy/bm	288 μJy/bm

Table 1.3: Comparison of peak polarization and rms for calibrator images with $D-$terms calculated per IF and per channel.

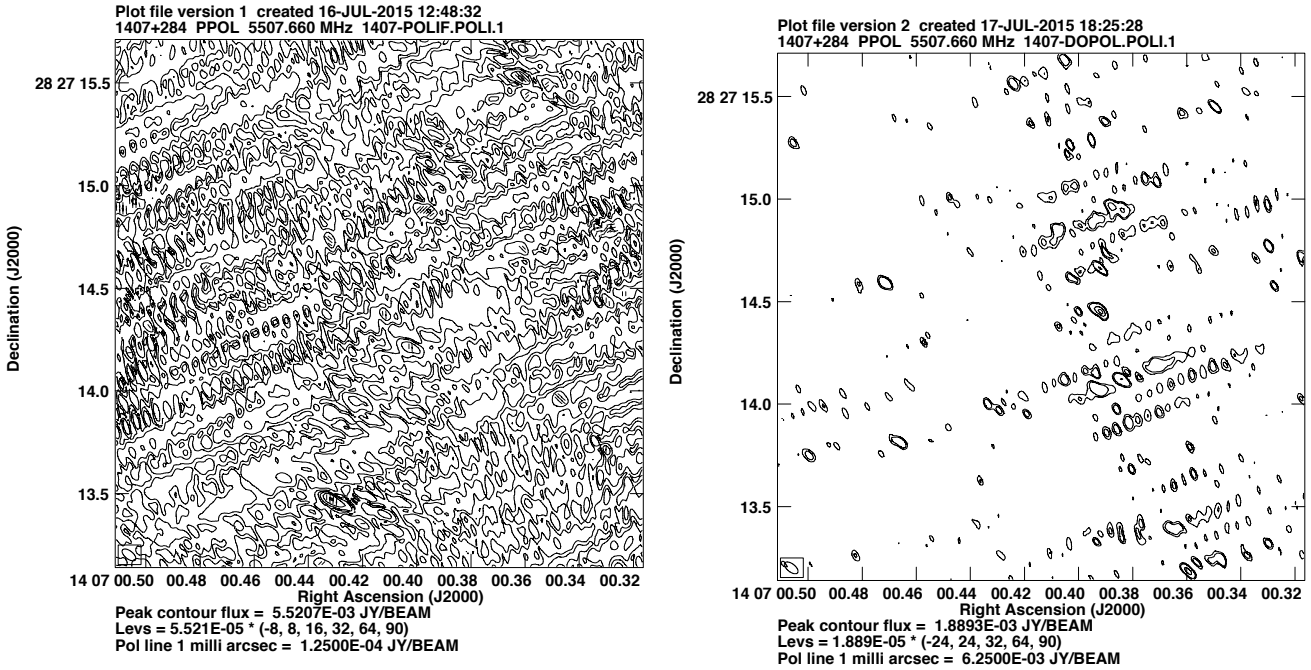

Figure 1.16: 1407+284 (zero-pol calibrator) with calibration done by integrating along the bandwidth (left) and for single channels (right). rms values for this image are given in table 1.3. For these two images, the lowest levels are of the same intensity. It can be seen that the rms improves by a factor of 4.

bandwidth). The effect of these corrections can be appreciated visually in figure 1.16.

1407+284 has zero polarization at 5 GHz, and so an ideal calibration in polarization should give no statistically significant polarization peak. Note that, for the left-hand values (single IF $D-$terms correction) gives a peak $\sim 13\sigma$, whereas for the right-hand values (single channel correction) the peak is also $\sim 13\sigma$. Both are high σ values that suggest that the correction is not ideal, but the single channel correction has a noise that is a factor of 4 lower, and is a better correction.

In figure 1.12(a), we can see that the polarization peak in 1407+284 *without* any instrumental correction is 93.2 mJy/bm. This is reduced by a factor of almost 17 for the single IF correction, and by a factor of 49 for the single channel correction. We can also see that the signal is almost evenly distributed along the whole image.

The second row of table 1.3 corresponds to the polarization angle calibrator 1331+305 (see fig. 1.17 for illustration). 1331+305 is a polarized source whose behaviour at 5 GHz is well-known. In this case, the source has actual polarization, which convolves with the instrumental polarization. This has a smearing effect, dispersing the localized polarization from the source to a larger surface

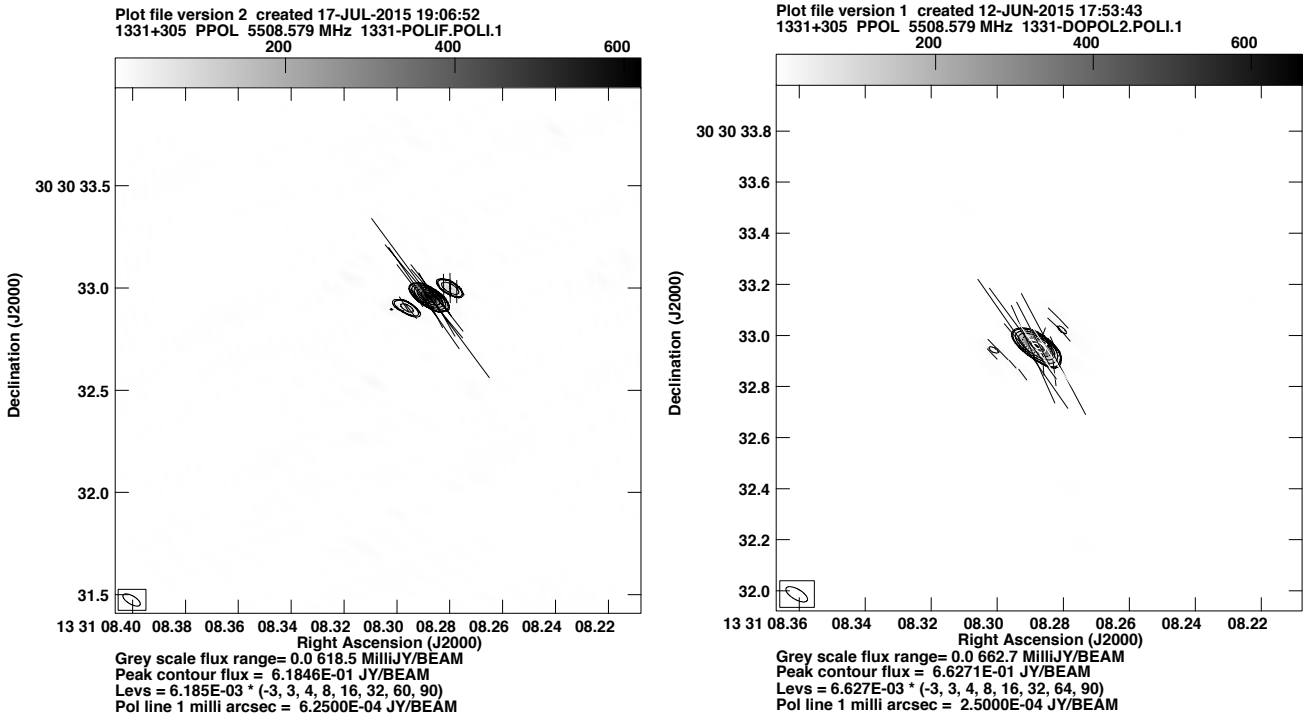

Figure 1.17: 1331+305 (polarization angle calibrator) with calibration done by integrating along the bandwidth (left) and for single channels (right). rms values for this image are given in table 1.3. In this case, the peak values are not as different as in the case of 1407+284. (Note that the frames are not the same for both figures.)

area. That is why, for 1331+305, the polarization peak is slightly *higher* for the single channel correction than for the global IF correction. The noise is a factor of 3.5 higher for the worse correction, meaning that the signal is sharper for the single channel correction.

The $D-$terms we have determined are plotted in figure 1.18a. For reference, the integrated values employed in the POLIF images (single IF polarization correction) are also given in 1.18b. Although, in the case of the integrated $D-$terms, their values are seemingly reasonable (with a maximum of the order of 30% for the Cambridge antenna), in the single-channel $D-$terms plot we see that some of these values are surprisingly high. Not accounting for the channels that have such high instrumental polarization contributions can result in a misleading polarization signal that we might (mistakenly) associate with the source. It is not just a matter of individual channels behaving in an unexpected way: the $D-$terms as seen in figure 1.18a also have a slope with frequency (especially steep for the first IF). There is a trend in the intensity of the $D-$terms along the bandwith, and so it is unreasonable to calculate a single $D-$term for all channels in an IF.

Since the calibration of polarization on a per-channel basis gives better results, the $D-$term values listed in 1.18a are the ones used to correct the phase calibrator and the target for polarization.

What we gather from this discussion is that the instrumental polarization can be very important, adding a substantial polarization flux to our data. Calibrating its contribution must be done in a per-channel basis. This is the procedure that will need to be performed in the future interferometers

with large bandwidths.

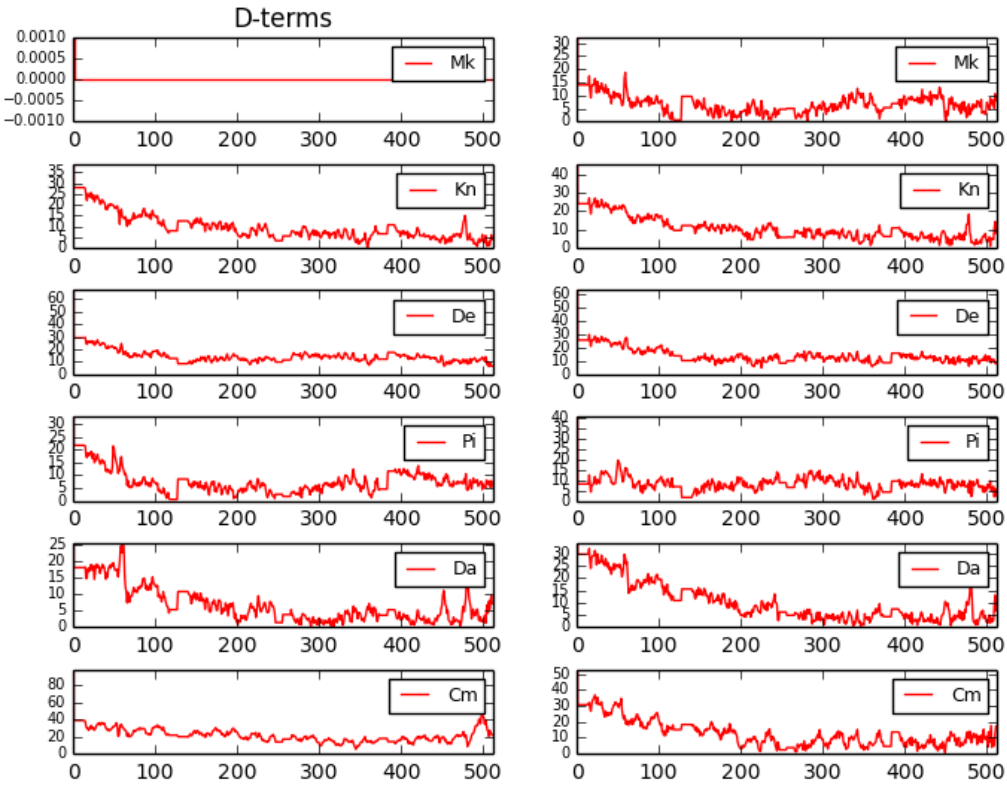

(a) $D-$term values are individual for each channel.

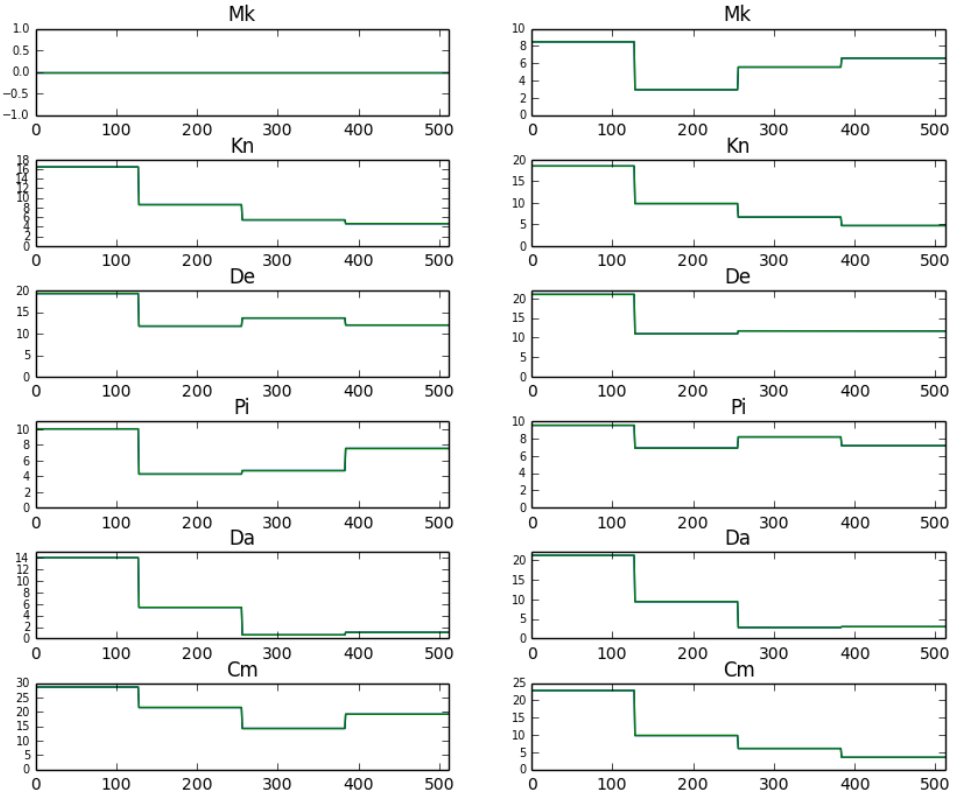

(b) 4 $D-$term values are used for the entire bandwidth.

Figure 1.18: $D-$terms per MHz, per antenna. Left is RCP and right is LCP.

Chapter 2

Gravitational Lenses and B1938+6648

Gravitational lensing occurs when a distribution of matter between a source and an observer bends the light from the source as it travels towards the observer, resulting in multiple images of the background astronomical object. It is a general relativity effect.

Maximum bending of the light takes place closest to the center of the lens, and so instead of a focal point, a gravitational lens has a focal line. If the source, lens, and observer lie in the same line, the light source will appear as a ring around the gravitational lens (an Einstein ring). If there is some misalignment, the source will be observed as an arc segment. The subclass of gravitational lensing where there are easily visible distortions is called *strong lensing*.

The target of this work, B1938+6648, is one of such objects. This source was discovered as part of the Jodrell Bank Centre for Astrophysics CLASS survey. The following description of the survey is from its website [15]:

> "It consisted of observations of flat-spectrum radio sources. Such objects are usually quasars and have very simple radio structures; they are typically point sources, and occasionally weak extended emission is visible. The point-like radio emission is thought to originate from the base of a relativistic radio jet [i.e., the core] in an active galaxy, which points more or less at the observer.
>
> The simplicity of these sources is useful for gravitational lensing searches. This is because any flat-spectrum radio source which has extended structure is a possible gravitational lens, as the extended structure could represent multiple images of a pointlike radio source, produced by the gravitational field of an intervening galaxy. (Usually, the intervening galaxy will not be seen in the radio map). In practice, a filtering operation, involving observations at successively higher resolutions with MERLIN and VLBI, was undertaken to separate genuine gravitational lenses from the cases where the extended structure was intrinsic to the quasar."

In [2] the authors examine the effect of a foreground gravitational lens in the polarization of a background object, and conclude that the polarization directions of photons in a beam propagating under the influence of a gravitational lens remain unaffected by the lens in most cases. The exception are lenses in very rapid rotation (such as a rapidly rotating black hole), and even then the direction of polarization is only rotated locally.

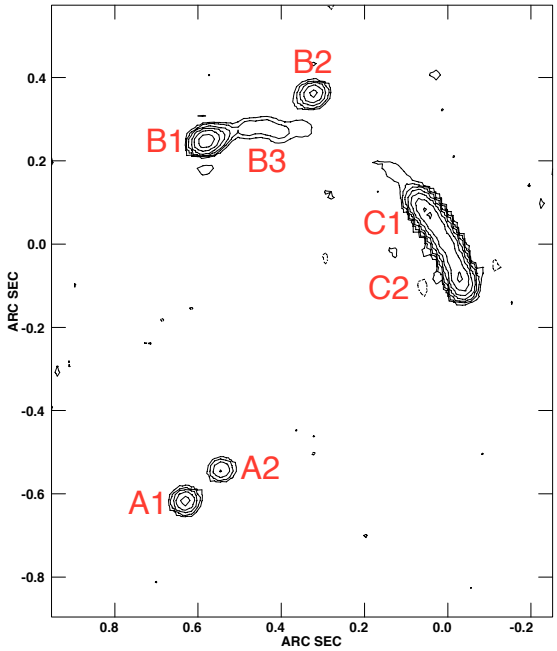

Figure 2.1: King *et al.* [7] MERLIN 5GHz image of B1938+6648. The restoring beam diameter is 40 mas. The contours plotted are logarithmic; the lowest positive contour is $3\sigma = 0.5$ mJy/beam. Noise level is $\sigma = 167\mu$Jy/bm.

Since the plane of polarization is not affected by gravitational lensing, polarization observations can play an important role in the discovery and analysis of gravitationally lensed sources. For instance, polarization measurements can provide evidence for what structures are copies of a single source, similarly to how spectral index measurements do. This is to say, multiple images of a given source should have similar spectral index, polarization degree, and polarization angle.

2.1 B1938+6648

King *et al.* [7] present the results of multifrequency radio observations of the lens B1938+6648, including VLA, MERLIN, and VLBI data. In the MELIN 5GHz image, they identify as dominant features an arc complex C and pairs of fairly compact components A and B (see figure 2.1). Combining spectral observations and polarization properties, Narashima and Patnaik [9] suggested that the unlensed model consists of two components: one is quadruply imaged to reproduce the features C1, C2, B1, and A1 in fig. 2.1, and the second is doubly imaged to produce A2 and B2. King *et al.* [7] agreed with this distinction, but argue that there must be some substructure with at least one of these components. They also presented a simple lens model of a potential with small ellipticity (as in lensing by galaxy) that is consistent with this configuration.

	A1	A2	B1	B2	B3	C1	C2	Total	Beam
MERLIN 5GHz									
peak flux (mJy/bm)	11. 9	4.2	32.6	10.5	2.7	48.9	47.9		
total flux (mJy/bm)	12.5	4.2	40	12	9	227 (C1+C2)		305	$0.04'' \times 0.04''$
eMERLIN 5 GHz									
peak flux (mJy/bm)	14.2	4.6	41.3	12.5	3.4	68.5	68.5		
total flux (mJy/bm)	15.4	4.7	52. 8	13.7	5.8	266.6 (C1+C2)		357	$0.040'' \times 0.096''$

Table 2.1: Flux of each component of gravitational lens B1938+6648. **MERLIN** values taken from [7]. **eMERLIN** data is from image 2.2. The rms for both observations is approximately the same, although the King *et al.* observations have three times the integration time of ours.

2.1.1 Intensity measurements

The data used in this work was taken continuously over 16 hours on Jan 13 2014 with eMERLIN. eMERLIN is a more sensitive instrument than its predecessor, MERLIN, whose data King *et al.* used for their analysis. Figure 2.2 is our version of the intensity image of B1938+6648 (the same as figure 2.1). The flux density values for each component are listed in table 2.1.

In general, the flux values measured in this work are higher than those measured previously by King *et al.* [7].The 17% increase in total flux is most likely due to the fact that the observations have been made in different epochs, and the unlensed source should be variable. The background source has a core-jet structure (which corresponds to the two components measured previously), and the morphology of the jet can easily vary in a timescale of years. The variability is mainly in flux density, but the relative position of the different components remains fixed.

2.2 Polarization measurements

The polarization vectors of lensed images are unaffected by the gravitational field of a lens. Thus, lensed images of the same source component should have the same percentage polarization ($\frac{\sqrt{Q^2+U^2}}{I}$) and polarization position angle ($\arctan \frac{Q}{U}$).

Our polarization values, along with those from previous work, are listed in table 2.2. In our work, the instrumental polarization has been measured more accurately, resulting in more reliable polarization measurements. Moreover, the source itself can have changed between both observations.

In their work, King *et al.* [7] agree with Narashima and Patnaik [9] in their classification of components A1, B1, C1, and C2 as being repeated images of a single source. They justify this in the following manner:

- The percentage polarizations of C1 and C2 are very similar at 1.612 GHz ($\approx 15\%$), at 5 GHz (14.3% and 15.3%, respectively), strongly indicating that C1 and C2 originate from the same lensing component.

- C1 and C2 have the same intrinsic polarization angles, supporting the assertion that they

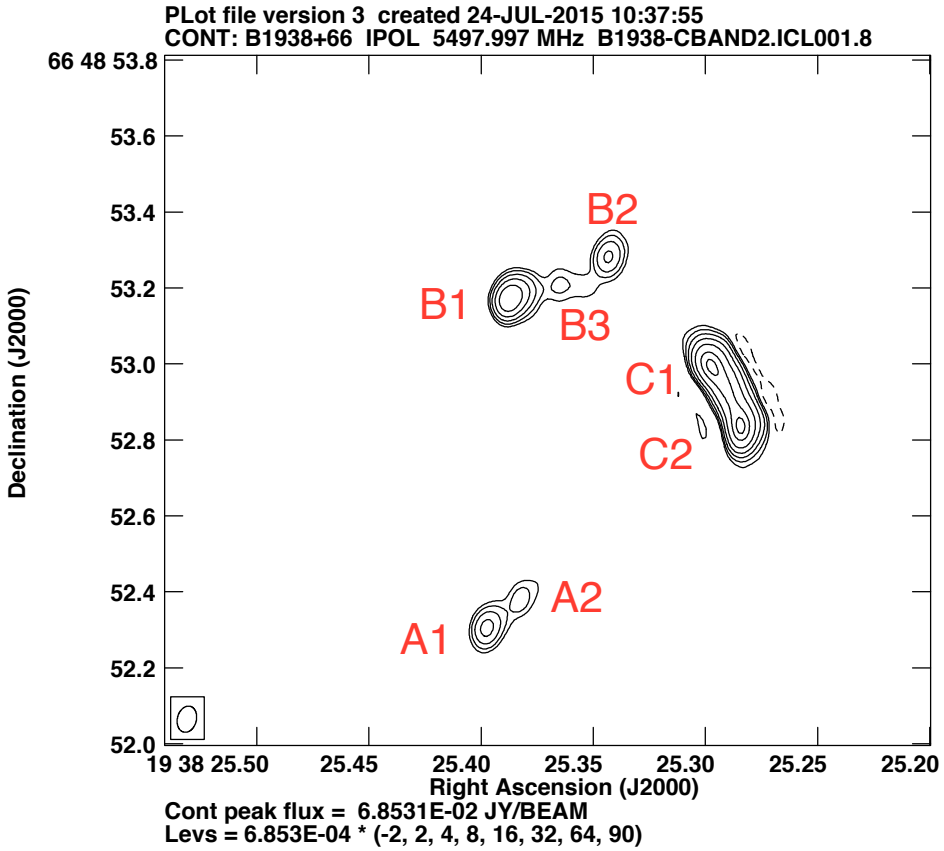

Figure 2.2: B1938+6648 in total intensity. This is a higher sensitivity version of figure 2.1. Here, rms = 102μ Jy/bm.

	A1	A2	B1	B2	B3	C1	C2
MERLIN 5GHz							
polarization angle			69.2			63	74
polarization percentage	8		6			14.3	15.3
eMERLIN 5GHz							
polarization angle	31		46			35	50
polarization peak (mJy/bm)	1.2		3.90			13.2	10.9
polarization flux (mJy/bm)	0.8		3.91			20.9	19.9
polarization percentage	5.1		7.8			14.7	16.2

Table 2.2: Polarization values of each component of gravitational lens B1938+6648. **MERLIN** values taken from [7]. Their noise level is 0.17 mJy/bm and their resolution is 40 mas. **eMERLIN** data is taken from image 2.3 **(b)** and has noise level 0.18 mJy/bm. The error in polarization angle is $\pm 10^{o}$ The small bump over C1 seen in figure 2.3 **(b)** has a polarization flux density of 1.5 mJy/bm.

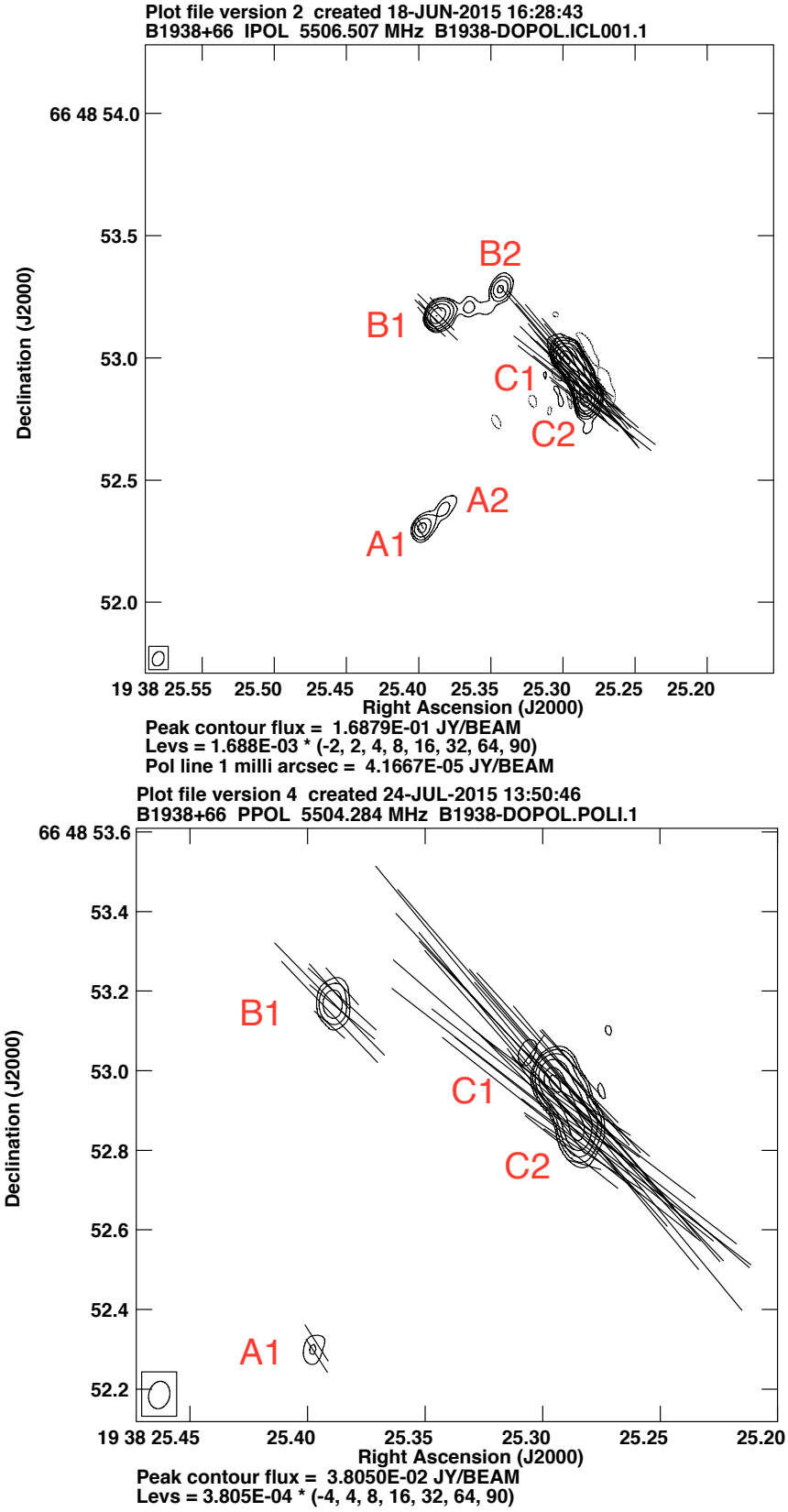

Figure 2.3: **(a)** Map of B1938+6648 in intensity with polarization vectors superposed, rms $= 1.02 \times 10^{-4}$ Jy/bm. **(b)** Map of B1938+6648 in polarization intensity $P = \sqrt{Q^2 + U^2}$ with polarization vectors, rms $= 1.75 \times 10^{-4}$ Jy/bm. Note that A2 and B2 are unpolarized.

originate from the lensing of the same component.

- The intrinsic PA of B1 is the same (to within errors) as that of C. Since B1 is also highly polarized like region C, and moreover B1 and C have similar spectral indices, it seems very likely that these are images of the same region of the source. However, since the percentage polarizations are not identical, there must be differential magnification altering the relative prominence of the subcomponents within each image. For example, a less polarized subcomponent could be less prominent in C than it is in B1.

- The polarization information on A1 is sparse. It is just detected at 5GHz and has a percentage polarization of 8 ± 2 per cent, similar to that of B1. There is no detection of polarization at other frequencies. Given the poorer signal-to-noise ratio this is still consistent with A1 having the same polarization properties as B1. Nothing can be said about its intrinsic polarization position angle.

They present polarization data at five different frequencies, and spectral indices for all six components, so their classification seems to be well-justified. Our results agree with their physical description.

It may appear unlikely that components with such different polarization percentages can be multiple images of a single source. This can be explained through the 'differential magnification' process mentioned above:

The background object is a quasar with a core-jet structure. This means that it is not a homogeneous source but rather has two components of different physical properties: the core and the jet. The core has a complex structure and higher opacity, whereas the jet component should be homogeneous and probably optically thin. Given the relative position of the source and the lens, it can happen that certain copies of the image reflect more of the core component or more of the jet component. This would result in a set of repeated images with different polarization and spectral properties.

The core is associated with the central engine of the source and its immediate surroundings. When enough matter (from, say, an accretion disk rotating around the black hole) falls into it, jets of expelled material can form, powered in part from the rotational energy of the black hole. These are highly collimated near the origin, and widen as they move forward and lose speed. The jets can have relativistic speeds; it is likely that the structure would have changed significantly from when the King *et al.* observations were taken twenty years ago, accounting for the different intensity and polarization values between their study and ours.

VLBI allows for the observation of very compact sources. Even so, the core of the quasar is unresolved and optically thick (meaning it can have self-absorption of part of the polarization), whereas the jet can be resolved, and is optically thin. The differences in the physical properties of these structures can explain that A1, B1, C1 and C2 have different polarization angle and percentage while allegedly being repeated images of the same source.

The second component, imaged doubly (A2 and B2), is unpolarized, in agreement with the suggestion that both are copies of a single object.

Conclusions

In this work we have discussed the steps taken to reduce polarization data in an interferometer experiment with a bandwidth of 512 MHz. We have used data from gravitational lens B1938+6648 taken with eMERLIN, a recently upgraded interferometer with baselines of up to 217 km. We have compared them to published results of the same source taken with the pre-upgrade telescope (MERLIN), consisting of the same antennas, meaning that the resolving power (the beam size) remains constant, and comparison of peak and noise levels are straightforward. A major difference between MERLIN and eMERLIN is that the upgrade has increased the available bandwidth by a factor of 8, improving the sensitivity of the images.

We have concluded that the polarization calibration should be performed on a per-channel basis, as opposed to per-IF (per-subband), since **(a)** the leakage polarization terms have a slope with bandwidth and **(b)** there are some channels that have unusually high leakage parameters. Not accounting for these features has the effect of smearing the signal and increasing the noise (by a factor of four in the case of our target source). In polarization measurements, where often the signal is of the order of the leakage parameters, it is of particular importance that the calibration of the instrument's contribution be determined very accurately.

We also studied in some detail the polarization properties of our source, gravitational lens B1938+6648. We note that there has been a slight increase in intensity from the published, earlier epoch, values. Our percentage polarization values largely agree with those measured previously, but the polarization angle measurements do not. Our data comes from a more sensitive instrument, and the calibration of instrumental polarization has been done taking narrower frequency ranges, and hence our values should be more reliable than the earlier ones. We agree with King *et al.*'s interpretation that the four polarized objects of the source and the two unpolarized ones are repeated images from a single polarized and a single unpolarized lensed object respectively.

A gravitationally lensed object maintains the polarization properties of the source. We explain the disperson in polarization percentage and angle as differential magnification of a core-jet structure, where the core is compact, optically thick, and can have a certain amount of self-absorption, whereas the jet is optically thin, and can move in a timescale of years. The change in morphology of the source due to the jet could, to some extent, explain the variation in polarization angles that we have measured with respect to earlier work, although the difference is most likely due to the different sensitivity of the interferometers and to instrumental polarization calibration errors.

Bibliography

[1] Condon, J.J. and Ransom, S.M. *Interferometers I.* Lecture notes from Essential Radio Astronomy, NRAO

[2] Faraoni, V. On the Rotation of Polarization by a Gravitational Lens. *Astron. Astrophys.* **272** 385-393 (1993)

[3] Fomalont, E., Perley, R. Calibration and Editing, Ch. 5 of *Synthesis Imaging in Radio Astronomy II.* APS Conference Series, Vol. 180, 1999

[4] Haverkorn, M. *Radio Polarisation and Magnetic Fields*, Lecture notes of the Radio Astronomy MSc. course, University of Leiden.

[5] Hamaker, J.P, and Bregman, J.D., Sault, R.J. Understanding Radio Polarimetry. I. Mathematical Foundations. *Astron. Astrophys. Suppl. Ser.* **117**, 137-147 (1996)

[6] Isella, A. *Radio Interferometry Basics*, Lecture notes of the Caltech CASA Radio Analysis Workshop. (2011)

[7] King, L.J. Browne, W.A., Muxlow, T.W., Narashima, D., Patnaik, A.R., Porcas, R.W., Wilkinson, P.N. Multifrequency radio observations of the gravitational lens system 1938+666, *Mon. Not. R. Astron. Soc.* **289**, Issue 2, 450-456 (1997)

[8] Lucas Lara Garrido. Estudio de cuasares y ncleos de radiogalaxias mediante la tcnica de radio interferometra de muy larga base: 3c395 y 3c382. Tesis doctoral. Universidad de Granada (1994)

[9] Narashima, D., and Patnaik, A.R. *Gravitational Lenses in the Universe* 31st Liege Int. Astroph. Coll., 295 (1993)

[10] Roberts, H.D., Wardle J.F.C., and Brown, L.F. Linear Polarization Radio Imaging at Miliarcsecond Resolution. *Astrophys. Journal* **427** 718-744, 1991

[11] Salter, C. *The Techniques of Radio Astronomy*, Lectures notes of the Arecibo Single Dish Summer School. (2013)

[12] Sault, R.J., Hamaker, J.P, and Bregman, J.D. Understanding Radio Polarimetry. II. Instrumental calibration of an interferometer array. *Astron. Astrophys. Suppl. Ser.* **117**, 149-159 (1996)

[13] Thompson, R.A., Moran, J.M., Swenson, G.W., *Interferometry and Synthesis in Radio Astronomy*, Second Edition. Chapter 4. Wiley-VCH (2004)

[14] Wardle, J.F.C., Roberts, D.H. *What You Can Learn from Polarization −Present and Future.* Compact Extragalactic Radio Sources, Proceedings of the NRAO workshop held at Socorro, New Mexico, February 11-12, 1994

[15] Jodrell Bank Center for Astrophysics CLASS Survey website `http://www.jb.man.ac.uk/research/gravlens/class/`

[16] e-MERLIN / VLBI National Radio Astronomy Facility `http://www.e-merlin.ac.uk`